



# Effect of dry-wet cycles on dynamic properties and microstructures of sandstone: Experiments and modelling

## Document Version

Accepted author manuscript

[Link to publication record in Manchester Research Explorer](#)

## Citation for published version (APA):

Pu, H., Yi, Q., Jivkov, A., Bian, Z., Chen, W., & Wu, J. (in press). Effect of dry-wet cycles on dynamic properties and microstructures of sandstone: Experiments and modelling. *International Journal of Mining Science and Technology*.

## Published in:

International Journal of Mining Science and Technology

## Citing this paper

Please note that where the full-text provided on Manchester Research Explorer is the Author Accepted Manuscript or Proof version this may differ from the final Published version. If citing, it is advised that you check and use the publisher's definitive version.

## General rights

Copyright and moral rights for the publications made accessible in the Research Explorer are retained by the authors and/or other copyright owners and it is a condition of accessing publications that users recognise and abide by the legal requirements associated with these rights.

## Takedown policy

If you believe that this document breaches copyright please refer to the University of Manchester's Takedown Procedures [<http://man.ac.uk/04Y6Bo>] or contact [uml.scholarlycommunications@manchester.ac.uk](mailto:uml.scholarlycommunications@manchester.ac.uk) providing relevant details, so we can investigate your claim.



# Effect of dry-wet cycles on dynamic properties and microstructures of sandstone: Experiments and modelling

Hai Pu<sup>a,b</sup>, Qingyu Yi<sup>a,†</sup>, Andrey P. Jivkov<sup>c</sup>, Zhengfu Bian<sup>d</sup>, Weiqiang Chen<sup>e</sup>, Jiangyu Wu<sup>a,f,g,\*</sup>

<sup>a</sup> State Key Laboratory of Intelligent Construction and Healthy Operation and Maintenance of Deep Earth Engineering, China University of Mining and Technology, Xuzhou 221116, China

<sup>b</sup> Key Laboratory of Xinjiang Coal Resources Green Mining, Ministry of Education, Xinjiang Institute of Engineering, Urumqi 830023, China

<sup>c</sup> Department of Solids and Structures, School of Engineering, University of Manchester, Manchester M13 9PL, UK

<sup>d</sup> School of Environment Science and Spatial Informatics, China University of Mining and Technology, Xuzhou 221116, China

<sup>e</sup> Department of Civil and Environmental Engineering, Rice University, Houston 77005, USA

<sup>f</sup> State Key Laboratory of High Performance Civil Engineering Materials, Jiangsu Research Institute of Building Science Co., Ltd., Nanjing 210008, China

<sup>g</sup> Department of Materials, University of Oxford, Oxford OX1 3PH, UK

**Abstract:** Underground pumped storage power plant (UPSP) is an innovative concept for space recycling of abandoned mines. Its realization requires better understanding of the dynamic performance and durability of reservoir rock. This paper conducted ultrasonic detection, split Hopkinson pressure bar (SHPB) impact, mercury intrusion porosimetry (MIP), and backscatter electron observation (BSE) tests to investigate the dynamical behaviour and microstructure of sandstone with cyclical dry-wet damage. A coupling FEM-DEM model was constructed for reappearing mesoscopic structure damage. The results show that dry-wet cycles decrease the dynamic compressive strength (DCS) with a maximum reduction of 39.40%, the elastic limit strength is reduced from 41.75 to 25.62 MPa. The sieved fragments obtain the highest crack growth rate during the 23rd dry-wet cycle with a predictable life of 25 cycles for each rock particle. The pore fractal features of the macropores and micro-meso pores show great differences between the early and late cycles, which verifies the computational statistics analysis of particle deterioration. The numerical results show that the failure patterns are governed by the strain in pre-peak stage and the shear cracks are dominant. The dry-wet cycles reduce the energy transfer efficiency and lead to the discretization of force chain and crack fields.

**Keywords:** Underground pumped storage power plant; dry-wet cycles; split Hopkinson pressure bar; macro and micro properties; FEM-DEM coupling model; damage characterization

## 1. Introduction

The secondary utilization of underground space in abandoned mines contributes to plenty of mine transition strategies. The innovative space utilization mode in recent years represented by underground pumped storage has attracted attention [1–3]. Considering the closure of global underground mines and the development of energy storage technologies, Underground Pumped Storage Power Plant (UPSP) is recommended as a viable solution that recycles the underground spaces of abandoned and supports the exploration of multi-energy power generation [4,5]. However, the common geological disasters in surface-pumped storage areas like landslides, earthquakes, rock microtremors, land loss etc., indicate the construction difficulty of UPSP, which particularly prompts concern about the stability and safety of underground reservoir spaces [6].

According to the existing examples of pumped storage hydropower with underground storage, the lower reservoirs are mostly located in stable sandstone, limestone or basalt formations [7,8]. The mine shafts, tunnels, or chambers based on hard rocks in abandoned mines tend to be the site selection for space reuse [9]. For the design of UPSP reservoirs, the long-term water circulation and repeated pumping shocks will significantly accelerate the degradation of surrounding rocks, and it not only refers to the progressive damage of water leaching in the static storing process but also includes the instant failure of impact loading in the dynamic pumping process [4,10]. Considering the varying soaking conditions in both the dead storage and the active storage of the reservoir, the water-rock interaction in the surrounding rock typically appears as cyclical water-saturated damage. In this aspect, the cyclical dry-wet treatments are commonly employed in indoor tests of progressive rock damage, which have been reported to decrease strength, stiffness, and deformation ability [11,12]. Some studies emphasized the chemical and corrosive processes such as dissolution, precipitation, hydration, etc., and concluded their crucial roles in the underlying weakening mechanism during the cyclical dry-wet process [13]. Additionally, the variations in mineralogical compositions and failure characteristics are also the typical results of cyclical dry-wet treatments and primarily influence the mechanical properties of rock materials [14,15]. However, the existing studies mostly focus on the macroscopic mechanical responses to the dry-wet cycles or provide qualitative explanations of the dry-wet damage mechanism, which are insufficient for the operational assessment of UPSP reservoirs.

---

Received

Received in revised form

\*Corresponding author1.

E-mail address: wujiangyu@cumt.edu.cn

†Corresponding author2.

E-mail address: qingyu.yi@cumt.edu.cn

Another significant aspect of UPSP space stability refers to the complex stress environment of the surrounding rock. This can be differentiated by the following characteristics, as currently speculated [4,10,16]: the cyclical loading due to the water fluctuations, the creep behaviour with confining pressure, and the dynamic impact induced by repeated pumping operation. Thereinto, the fatigue failure resulting from cyclic loading can stem from the loosening and decohesion of the rock grains under repetitive stress [17,18]. Creep phenomena exhibit an apparent time-dependent behaviour and can be characterized by the typical deformation-rate stages, it relates to the long-term stability of underground reservoirs [19]. Some researchers believe that these two factors are the main reasons for the stress corrosion, which imperceptibly threatens the operation safety of UPSP. In contrast, the dynamic impact presents a completely different failure process, which means that in addition to the conventional phenomena of rock dynamic responses (e.g. strain-stress behaviour, strain rate enhancement effect, dynamic failure patterns), the accumulation and evolution of cyclical dry-wet damage under dynamic disturbance will be significantly accelerated and affect the initial stability of UPSP reservoirs [20]. For this point, there are few studies on the quantifiable method of cyclical dry-wet damage, and their evolution and distribution features under rapid deformation are still unknown.

With the advance of secondary space utilization in abandoned mines, the innovative development mode represented by UPSP will cause a new challenge for the dynamic performance and durability of underground reservoirs. The microscopic failure caused by circulating water erosion might have a profound influence on the macroscopic mechanical properties of rock materials, and the progressive damage of pore structure, mineral components, and micromorphology needs to be quantitatively evaluated with more reliable prediction techniques. Therefore, this paper studies the effect of dry-wet cycles on the dynamic mechanics and microstructure of sandstone. The ultrasonic detection, split Hopkinson pressure bar (SHPB) impact, mercury intrusion porosimetry (MIP) tests, and backscatter electron (BSE) observations were carried out to discuss the hydrous degradation characteristics of sandstone. The micro-damage and macro failure features induced by dry-wet cycles are quantitatively compared, and the damage distribution and energy evolution under dynamic impact are further analysed based on the continuous-discrete coupling numerical technology. The results provide the reference for the safety and stability assessment of UPSP reservoirs and contribute to the reconstruction engineering of abandoned mines.

## 2. Materials and methods

### 2.1. Materials and samples

The sandstone samples used in this paper were taken from Junan Mine in Shangdong Province, China. The samples' density was 2.63 g/cm<sup>3</sup>, and their mineral composition is shown in Table 1 and Fig. 1. The high content of feldspar (albite) and quartz in the sandstone provides sufficient strength for performing dry-wet cycle tests. The illite and montmorillonite, which are highly hydrophilic and easy to disintegrate in water, account for 26.9% of the sandstone.

According to the standards of International Committee on Rock Dynamics [21], all samples were processed into  $\Phi 50 \times 50$  mm cylinders, the height error was controlled within 0.5 mm, the surface roughness was less than 0.1 mm, and the deviation of normal to terminal face was less than 0.25°.

**Table 1** The compositions of sandstone.

Minerals	Microcline	Illite	Montmorillonite	Albite	Quartz	Calcite
Content (%)	12.3	21.7	5.2	24.1	26.2	10.5

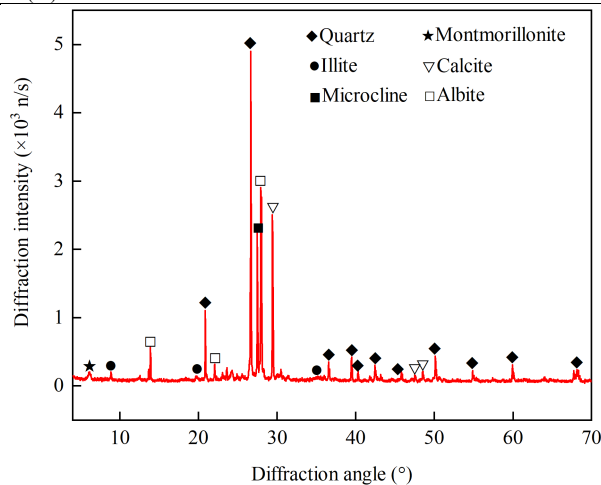


**Fig. 1.** X-ray diffraction spectrums of sandstone.

## 2.2. Drying-wetting procedure

The standard for indoor dry-wet cycle tests is based on the cyclical dry-wet method proposed by Khanlari et al. [22]. One dry-wet cycle comprises samples saturation in water at  $25\pm 5$  °C for 24 h and samples drying in a drying box at  $110\pm 5$  °C for 24 h. The samples were designed to endure a maximum of 40 dry-wet cycles, with additional 6 h allocated for natural cooling of the sandstone following each drying process. Fig. 2 shows the equipment used for realizing the dry-wet procedure. The 30 sandstone samples were divided into 5 groups, and each group was set for 0, 10, 20, 30 and 40 times dry-wet cycles. During the cyclical dry-wet process, the ultrasonic pulse velocity (UPV) for each sample was recorded using an ultrasonic velocimeter. Following the dry-wet cycles test, four samples from each group underwent mechanical tests and the remaining two samples were allocated for microscopic tests. The surface morphology of samples with different numbers of dry-wet cycles is shown in Table 2 together with other test parameters.

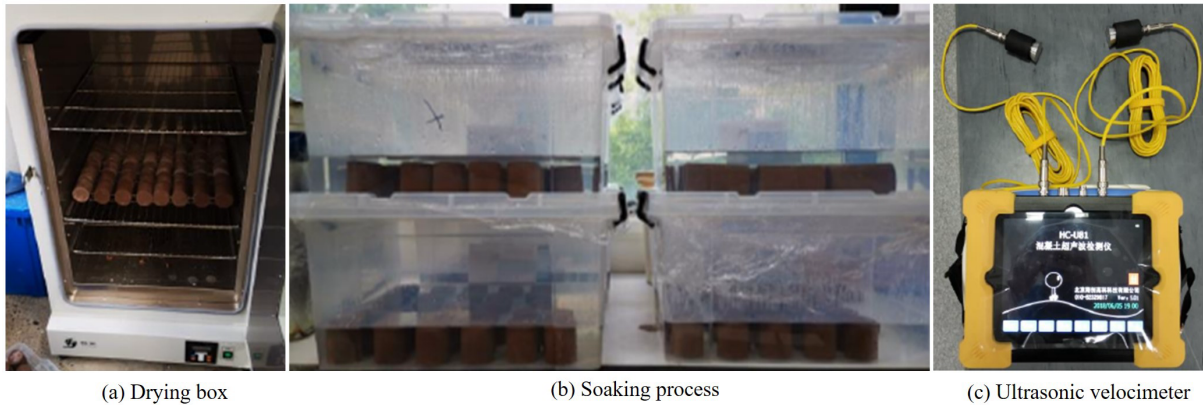
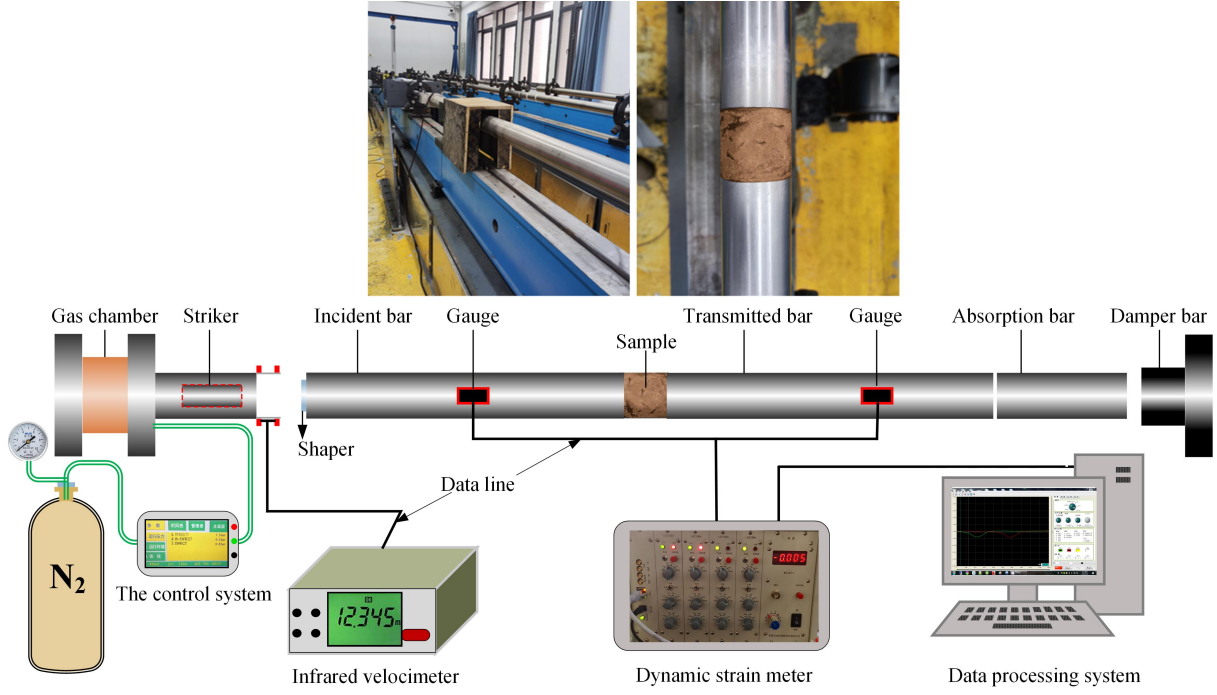


Fig. 2. Equipment for dry-wet cycles.

## 2.3. Dynamic impact test

Dynamic compression tests were conducted on sandstone samples after different dry-wet cycles using a multi-functional SHPB test platform at China University of Mining and Technology. The SHPB system, shown in Fig. 3, has three components: a power generation device, a load transfer device, and a data acquisition device. The power generation device includes a striker, a high-pressure gas chamber, and a control system. The impact load of the striker can be controlled by inputting air pressure, and the impact velocity is determined by an infrared velocimeter at the end of the chamber. The load transfer device includes an incident bar, a transmitted bar, and an absorption bar. When the striker contacts the incident bar, an incident stress wave is generated and transmitted to the sample. When this wave reaches the sample end, a fraction of its energy is transferred to the transmitted bar in the form of a transmitted wave, while the remaining energy is reflected through the sample to the incident bar in the form of the reflected wave. The residual energy of each impact test is absorbed by the absorption bar and damper bar. The data acquisition device includes strain gauges mounted on the incident and transmitted bars, LK2109A ultra-dynamic strain meter and an LK2400N data acquisition instrument so that the acquired data is recorded in a computer. All bars used in the system of 50 mm diameter, made of alloy steel with density of  $7.821 \text{ kg/cm}^3$ , elastic modulus of 206 GPa, and p-wave velocity of 5123 m/s.



**Fig. 3.** Schematic diagram of SHPB test system.

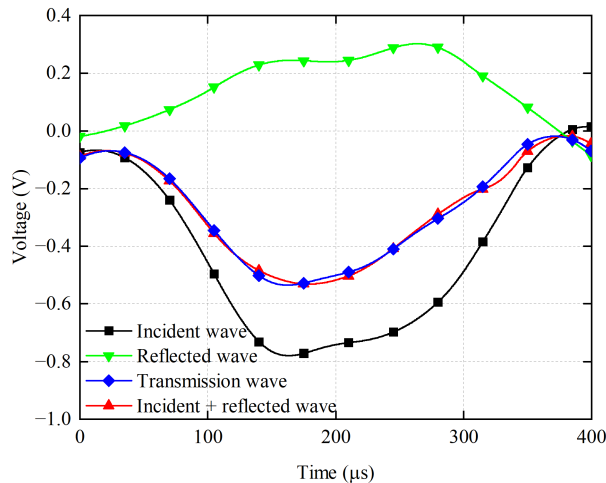
To study the effect of different dry-wet cycles on the dynamic mechanical properties, all tests need to be conducted in the range of dynamic loading strain rate ( $>100 \text{ s}^{-1}$ ). After adequate testing, 0.3 MPa was set as a suitable air pressure to meet this condition. Before each impact test, a shaper was placed at the impact end of the incident bar, and vaseline was uniformly applied on the interfaces between the samples and the two bars to minimize the end-face friction effect. The dynamic stress equilibrium of the samples was validated by plotting the time-history of the three stress waves during the impact process as shown in Fig. 4. The sum of the incident and reflected waves aligns with the transmitted wave, indicating that the impact process satisfies the stress equilibrium conditions. Table 2 gives the specific impact test schemes. The test data were processed with the three-wave method [23], and the peak value of  $\sigma(t)$  was noted as the dynamic compressive strength (DCS).

$$\dot{\varepsilon}(t) = \frac{C}{L_0} [\varepsilon_i(t) - \varepsilon_r(t) - \varepsilon_t(t)] \quad (1)$$






$$\varepsilon(t) = \frac{C}{L_0} \int_0^t [\varepsilon_i(t) - \varepsilon_r(t) - \varepsilon_t(t)] dt \quad (2)$$

$$\sigma(t) = \frac{A}{2A_0} E [\varepsilon_i(t) + \varepsilon_r(t) + \varepsilon_t(t)] \quad (3)$$

where  $C$  and  $E$  represent the p-wave velocity and the elastic modulus of the bars, respectively;  $L_0$  is the sample length;  $A$  and  $A_0$  represent the cross-section areas of the bars and the samples, respectively;  $\varepsilon_i(t)$ ,  $\varepsilon_r(t)$ , and  $\varepsilon_t(t)$  are the incident strain, reflection strain, and transmission strain, respectively;  $t$  is the loading time of stress wave.



**Fig. 4.** Dynamic stress equilibrium curve.**Table 2** Experimental scheme.

Sample number	Dry-wet cycles ( <i>n</i> )	Impact pressure (MPa)	Impact velocity (m/s)	Mean strain rate (s <sup>-1</sup> )	Surface morphology
0-0.1	0	0.3	5800	40.20	
0-0.2			5800	40.72	
0-0.3			5700	39.84	
0-0.4			5800	40.28	
1-0.1	10	0.3	5700	40.14	
1-0.2			5900	40.21	
1-0.3			5700	39.62	
1-0.4			5500	39.11	
2-0.1	20	0.3	5800	40.16	
2-0.2			5800	39.82	
2-0.3			5800	39.91	
2-0.4			5900	40.37	
3-0.1	30	0.3	5800	40.91	
3-0.2			5900	41.82	
3-0.3			5800	39.91	
3-0.4			5700	39.65	
4-0.1	40	0.3	5500	39.42	
4-0.2			5700	39.84	
4-0.3			5800	39.94	
4-0.4			5800	40.03	

## 2.4. Microstructure characterisation

The pore space of sandstone after different dry-wet cycles was characterized by MIP using Auto Pore V9600 mercury porosimeter from Micrometrics, USA. According to the operating specification, the mercury intrusion pressure range was set from 0.1 Psia to 61000 Psia to obtain the characteristics of micropores, mesopores, and coarse pores with diameters  $10^{-3}$ – $10^3$   $\mu\text{m}$ . The intrusion pressure rate of mercury injection was set at 0.1 Psia/s to ensure that all pores were in a static loading process. In parallel, BSE imaging of the sandstone samples was performed using Quanta™ 250 scanning electron microscope from Thermo Fisher Scientific, USA. This allowed for studying the effect of dry-wet cycles on the microscopic morphology and grain structure of sandstone.

## 3. Experimental results and discussion

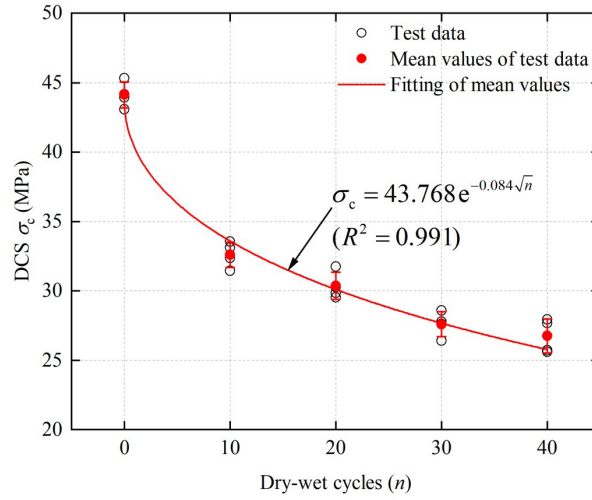
### 3.1. Dynamic strength

Fig. 5a shows the effect of dry-wet cycles on the DCS of sandstone. Increasing wet-dry cycles lead to decreasing mean DCS values from 44.12 MPa at 0 dry-wet cycle to 26.74 MPa after 40 dry-wet cycles; this is 39.40% reduction of the dynamic compressive strength. Ultrasonic technology offers a non-destructive approach to determining the strength variation of rock materials which is suitable for both field and indoor experiments [24]. It relies on establishing a relationship between the ultrasonic p-wave velocity (UPV) and the compressive strength. Fig. 5b shows the effect of the dry-wet cycles on the UPV of sandstone samples. Mean values were considered to eliminate the microstructural variations between the samples and potential measurement errors. The results show that UPV is a monotonically decreasing function of dry-wet cycles. Fitting the mean values provides an exponential decay curve with a coefficient of determination of 0.992, as depicted in the figure. Fig. 5c shows the relationship between UPV and DCS, confirmed by the exponential growth formula with a coefficient of determination 0.953. The results highlight the strong impact of the dry-wet cycles on the bearing capacity of sandstone validated by the ultrasonic technology due to the high correlation between DCS and UPV. It should be mentioned that these relationships are typically presented with exponential functions  $v = Ae^{Bn} + C$  and  $\sigma_c = \xi_{c1} e^{\xi_{c2} v}$ . According to these forms, UPV could approach zero when the dry-wet cycles approach infinity only when  $C=0$ , and if UPV approaches zero, the DCS becomes constant  $\xi_{c1}$ . This situation is not confirmed experimentally [25], suggesting that modification of the functions is necessary. The results presented here support the following modified exponential fitting functions:

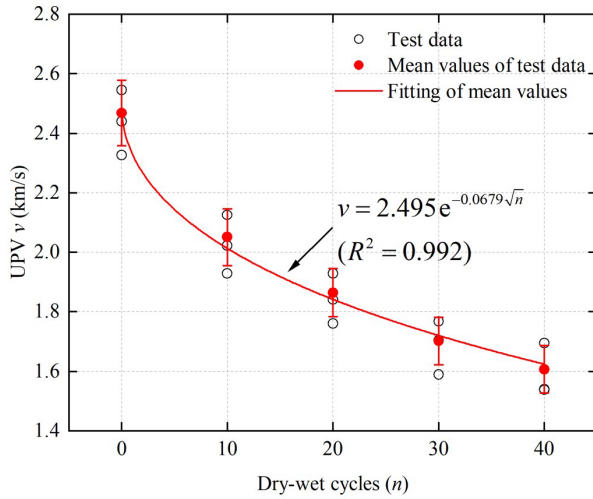
$$v = Ae^{B\sqrt{n}} \quad (4)$$

$$\sigma_c = \xi_{c1} e^{\xi_{c2} v} - \xi_{c1} \quad (5)$$

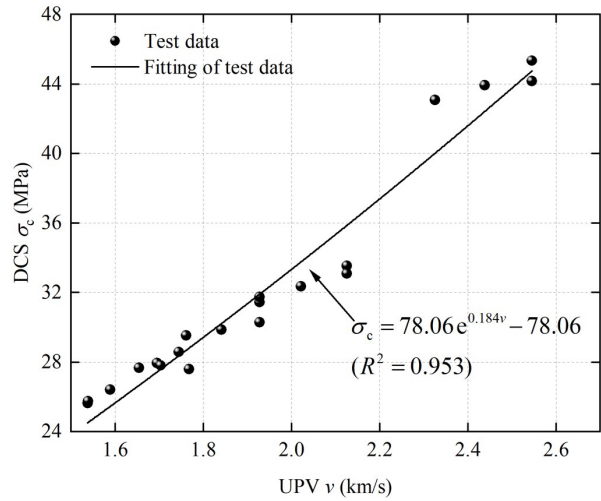
where  $v$  is the measured UPV,  $\sigma_c$  is the experimental DCS; A and B,  $\xi_{c1}$  and  $\xi_{c2}$  the fitting parameters.



(a) Dynamic compression strength versus dry-wet cycles



(b) P-wave velocity versus dry-wet cycles



(c) Dynamic compression strength versus p-wave velocity

**Fig. 5.** Characterization parameters of sandstone in different dry-wet cycles.

The proposed relationship between UPV and DCS defines a strength prediction model for sandstone; the difference between the experimental and the predicted values of DCS is shown in Fig. 6. All experimental DCS values are predicted with good accuracy within 10% error. The distribution of predicted values is less scattered for low experimental DCS values, indicating that the strength prediction model has better accuracy for the samples after dry-wet damage. Wu et al.'s work [25] came to a similar conclusion that the exponential model based on UPV has higher accuracy in predicting low compressive strength, and it can be improved by adding more detailed parameterization work to increase the accuracy in the high strength range. The results support the conclusion that the exponential model is suitable for predicting lower strengths of sandstone after cyclic dry-wet process.

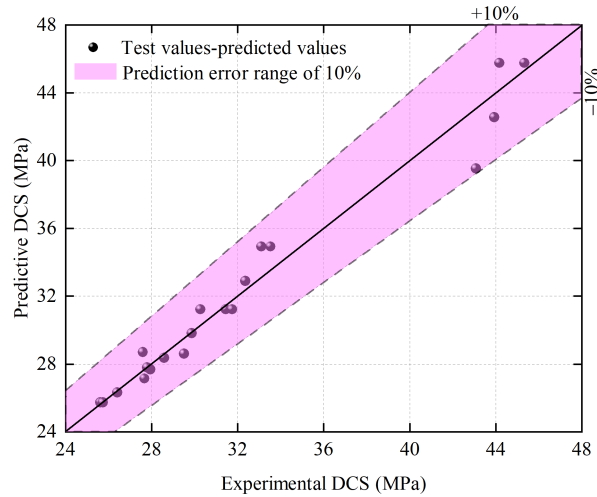


**Fig. 6.** Predictions of dynamic compressive strengths of sandstone.

### 3.2. Strain-stress behaviour

The results from SHPB dynamic impact tests are used to calculate the strain and stress in the samples by Eqs.(1)–(3). Fig. 7 shows typical strain-stress curves of sandstone under different dry-wet cycles. The deformation at each dry-wet stage is divided into three stages using four points: A, B, C, and D. The first stage, between points A and B, is characterized by a linear stress-strain relation, indicating elastic deformation. The second stage, between points B and C, is characterised by non-linear stress-strain behaviour, like strain-hardening in metals. During this stage the sandstone undergoes plastic-like deformation due to the expansion of micropores and cracks [26]. The third stage, between points C and D, is characterized by strain-softening, i.e., stress reduction with increasing strain, until complete failure of the samples. During this stage, the defects enlarged or generated during the second stage are coalescing into larger defects causing eventual failure [27]. Point B marks the elastic limit, point C marks the peak stress, and point D marks the failure.

The strain-stress behaviours in Fig. 7 show further that increasing dry-wet cycles lead to decreasing elastic limit stress (point B) from 41.75 MPa for sandstone at 0 dry-wet cycle to 25.62 MPa for sandstone after 40 dry-wet cycles. At the same time, the elastic limit strain first decreases and then increases with a fluctuation in the range of 0.14% to 0.25%. The initial stiffness values (slopes of the AB linear segments) are nearly constant between 0 and 30 dry-wet cycles, while a significant stiffness reduction is seen after 40 dry-wet cycles. This suggests that the cyclic dry-wet process can weaken the intergranular bonding of minerals and lead to a deterioration structure. As the number of dry-wet cycles reaches the range of 30 to 40, a stiffness transition occurs inside the specimen and leads to a substantial reduction of the elastic modulus of sandstone. As for the plastic deformation stage, the plastic strain between B and C gradually decreases with the increase of dry-wet cycles, and the value reduces from 0.14% at 0 dry-wet cycle to 0.04% after 40 dry-wet cycles. Similarly, the increment of stress in the plastic segment BC decreases from 2.37 MPa for sandstone at 0 dry-wet cycle to 1.12 MPa after 40 dry-wet cycles. The relative value of plastic stress and peak stress falls from 5.37% at 0 dry-wet cycle to 4.19% after 40 dry-wet cycles, while the relative value of strain drops from 35.90% to 17.39% during this period. This indicates that the effect of cyclic dry-wet processes on plastic strain far exceeds that of plastic stress, which diminishes the amount of plastic mineral components such as clay minerals and induces more micropores and cracks so that the plastic deformation ability of sandstone continuously decreases.



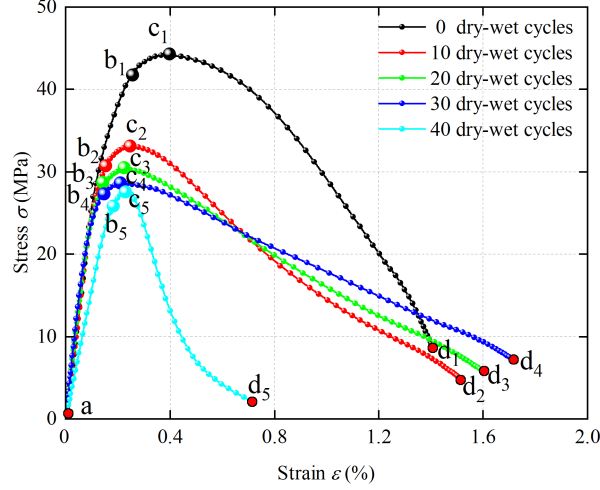


**Fig. 7.** The effect of the dry-wet cycles on the strain-stress behaviour of sandstone.

It should be noted that the dry-wet cycling test conducted in this study involves both the cyclical dry-wet process and variations in circulating temperature, which jointly affects the stiffness, the elastic limit stress, and the plastic deformation ability of sandstone samples. In this context, the repeated water saturation of rock materials is widely recognized as a primary factor causing structural damage [28]. It not only triggers cyclic tensile and compressive stresses within rocks but also leads to the formation of numerous microscopic defects as pore water evaporates and minerals dissolve [29]. Furthermore, the impact of circulating temperatures on rock materials cannot be overlooked, as it can lead to internal stress fatigue and regional temperature damage [30]. These factors continue to affect the mechanical performance of rocks in dynamic tests and will be further confirmed in the following sections.

### 3.3. Dynamic failure characteristics

Fragmentation characteristics can reflect the effect of dry-wet cycles on the dynamic behaviour of sandstone. To facilitate the fractal calculation of particle packing and the full utilization of rock fragments, the crashed fragments of each sandstone sample are divided into five size intervals: 0.0–1.0, 1.0–2.5, 2.5–5.0, 5.0–10.0 and 10.0–20.0 mm; this is illustrated in Fig. 8 for one sample. The parameter used to quantify the fragmental degree of specimens in different dry-wet cycles is the fractal dimension  $D_f$ , which is calculated with the following equations [31]:

$$P_i = \frac{M_i}{M_t} = \frac{d_i^{3-D_f} - d_{\min}^{3-D_f}}{d_{\max}^{3-D_f} - d_{\min}^{3-D_f}} \quad (6)$$

where  $d_i$  is the fragment diameter of the current interval;  $d_{\min}$  and  $d_{\max}$  the minimum and the maximum fragment diameters, respectively;  $M_i$  the mass of fragments passing through a sieve with spacing  $d_i$ - $d_{\min}$ ;  $M_t$  the total mass of fragments; and  $P_i$  the mass fraction defined as the ratio of  $M_i$  to  $M_t$ . When  $d_{\min}^{3-D_f} \rightarrow 0$ , Eq. (6) becomes [32]:

$$\lg\left(\frac{M_i}{M_t}\right) \propto (3 - D_f) \lg\left(\frac{d_i}{d_{\max}}\right) \quad (7)$$



**Fig. 8.** The crashed fragments of a sample after SHPB impact.

The measured and calculated parameters are given in Table 3. The linear fits between  $\lg(M_i/M_t)$  and  $\lg(d_i/d_{\max})$  used to determine  $D_f$  by Eq. (7) are shown in Fig. 9a. With the increase of dry-wet cycles, the slope of the linear fits  $k$  decreases from 0.964 at 0 dry-wet cycle to 0.778 after 40 dry-wet cycles with a reduction of 19.3%. Correspondingly, the fractal dimension  $D_f$  increases from 2.036 to 2.247 with the increase of dry-wet cycles. This shows that the cyclic dry-wet processes induce structural changes that disrupt the sandstone skeleton, resulting in a

higher degree of fragmentation and worse bearing performance. The apparent embrittlement of sandstone by the dry-wet cycles can be considered as fatigue. The dependence of the fractal dimension on the number of dry-wet cycles is shown in Fig. 9b. The results suggest that the rate of specimen fragmentation firstly increases and then decreases with the increase of dry-wet cycles.

**Table 3** The fractal dimension of sandstone under different dry-wet cycles.

Dry-wet cycles ( $n$ )	Total mass $M_t$ (g)	Accumulative mass $M_i$ (g)					Fitting slope ( $k$ )	Fractal dimension ( $D_f$ )
		0–1.0 mm	0–2.5 mm	0–5.0 mm	0–10.0 mm	0–20.0 mm		
0	179.31	2.33	5.19	9.45	21.53	40.42	0.964	2.036
10	166.67	2.69	5.41	11.09	22.81	43.15	0.944	2.056
20	174.31	4.16	8.79	17.91	29.63	61.72	0.895	2.105
30	163.69	7.64	15.64	26.20	41.92	82.57	0.778	2.222
40	181.70	11.34	20.85	35.12	59.09	109.24	0.753	2.247

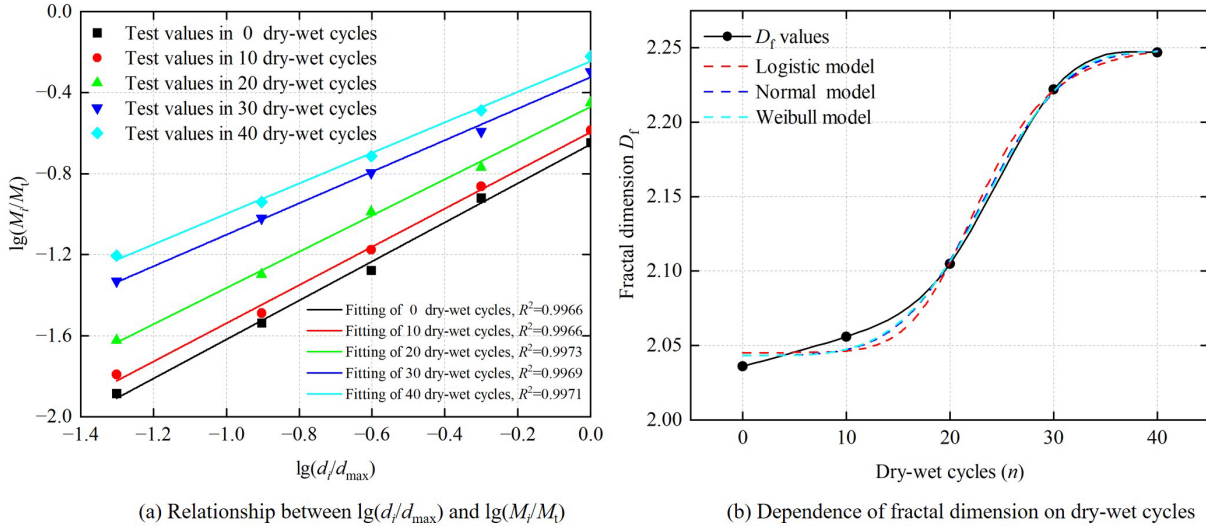


**Fig. 9.** The effect of the dry-wet cycles on the dynamic failure characteristics of sandstone.

Early statistical models for fragmentation of brittle materials have been reviewed by Åström et al. [33]. They emphasized the role of the exponential function for describing instantaneous fragmentation such as rock blasts. Weibull model, together with other statistical models using the exponential function, has been widely employed in the statistical analysis of rock damage and fragmentation prediction. The predictive ability of three typical statistical models: the logistic model, the normal model, and the Weibull model, in terms of fractal dimension is assessed here. The fits of the three models to the experimental data are shown in Fig. 9b. Table 4 provides the fitting parameters and the coefficient of determination. Based on the physical interpretation of the logistic model [34], the dry-wet cycle test is anticipated to elevate the fractal dimension of fragments to a peak value of 2.253, resulting in a  $D_f$  change of 0.208, and the most significant increase in fragmentation occurs during the 23<sup>rd</sup> dry-wet cycle. The normal model predicts the peak  $D_f$  value to be 2.249 with an increment of 0.206, and the mean value appears near the 23<sup>rd</sup> dry-wet cycle as well. The Weibull model predicts that the mean life of rock under the influence of dry-wet cycles is 25 cycles, and damage probability continues to increase with the dry-wet cycles. This indicates that the cyclic dry-wet process cannot change the critical interval of rock fragments, and the influence of dry-wet cycles on rock fragmentation is predictable under known impact conditions.

Since the coefficient of determination is all above 0.99, the three types of models can be employed to predict the rock fragmentation distribution. However, the three models have their own advantages in application scenarios due to the difference in mathematical principles, which can be reflected by  $A_2$  parameters. In this section, the logistic model and normal model are more suitable for the probability prediction of overall fragmentation distribution, while the Weibull model is more beneficial for predicting the service life of rock elements. In this aspect, the practical application of the three models needs to be further determined with more experiments.

**Table 4** Prediction models of fragmental fractal dimension.

	Fitting equation	Feature parameter				$R^2$
		$A_0$	$A_1$	$A_2$	$A_3$	
Logistic model	$D_f = A_0 - \frac{A_1}{1 + (n/A_2)^{A_3}}$	2.253	0.208	23.007	6.390	0.99509
Normal model	$D_f = A_0 + A_1 \times \text{normcdf}\left(\frac{n-A_2}{A_3}\right)$	2.043	0.206	23.127	6.377	0.99624
Weibull model	$D_f = A_0 + A_1 \times \text{wbldcdf}(n, A_2, A_3)$	2.043	0.205	25.336	4.180	0.99645

### 3.4. Pore structure

The pore structure of rock materials is highly susceptible to saturated dry-wet cycles. Fig. 10 shows the effect of dry-wet cycles on the cumulative pore volume of sandstone samples. According to Fig. 10a, the mercury intrusion volume increases with the dry-wet cycles, and this trend is evident across all pore size intervals. It indicates that the porosity of sandstone keeps increasing with the dry-wet cycles. The sandstone skeleton becomes sparse during the cyclical dry-wet process, which leads to the changes in strain-stress behaviour observed after the SHPB tests. For detailed analysis of the pore space, the pores are classified as micropores with diameters  $<10^2$  nm, mesopores with diameters  $10^2-10^4$  nm, and macropores with diameters  $>10^4$  nm [35]. Fig. 10b shows the pore size distribution of sandstone samples in different dry-wet stages. The pores in each dry-wet cycle are mainly distributed around  $10^4$  nm, which corresponds to the transition from mesopores to macropores. With the increase of dry-wet cycles, the fraction of pores around  $10^4$  nm and above firstly increases and then decreases. This indicates that the saturated pores during the cyclic dry-wet process are primarily macropores of  $10^4$  nm and above. In the early dry-wet stage, the macropores are gradually enlarged because of repeated pore pressure and mineral dissolution. With the progress of dry-wet cycles, the evaporation of pore water, the development of cracks, and the precipitation of soluble minerals disrupt the original pore structure and distribution, and the fraction of macropores continuously decreases in the late dry-wet stage.

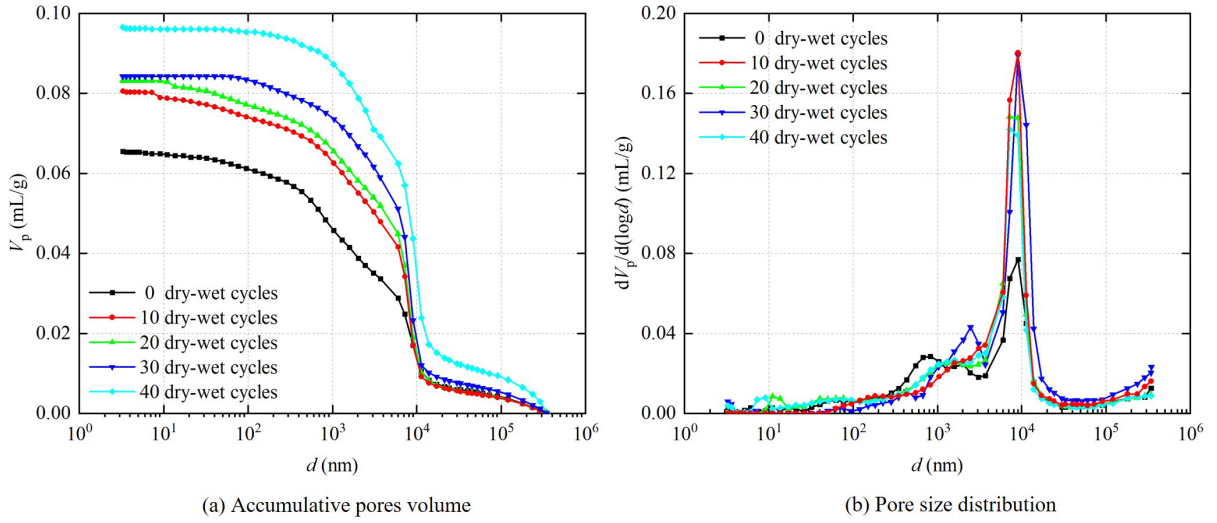


**Fig. 10.** The effect of dry-wet cycles on the pore structure of sandstone.

Further analysis of the pore space structure can be performed by calculating the pore fractal dimension  $D_p$ . Suitable for this work is the Neimark model, which is a solid surface fractal method for porous media under non-wetting fluid capillary invasion conditions [36]. The model assumes that the interface between a pore and the adjacent fluid is a surface of constant curvature. The area and curvature of the interface under capillary equilibrium conditions are derived from thermodynamic relations. These effectively describe the distribution characteristics of micro-, meso- and macro-pore sizes in MIP test. The Neimark model is employed here to calculate the pore fractal dimensions at different dry-wet stages. The liquid-solid interface area of the mercury intrusion can be expressed as:

$$S = \frac{-1}{\gamma \cos \theta} \int_0^{V_p} P dV \quad (8)$$

where  $S$  is the area of liquid-solid interface;  $\gamma$  the surface tension of mercury and  $\theta$  stands for the contact angle between the mercury and the pore surface; and  $V_p$  the intrusion volume of the capillary tubes at pressure  $P$ .

When the solid surface of porous media has a fractal property, the liquid-solid interface area  $S$  and the pore diameter  $d_p$  satisfy the relationship:

$$S \propto d_p^{2-D_p} \quad (9)$$

where  $d_p$  is the pore diameter at pressure  $P$ ; and  $D_p$  the fractal dimension with values between 2(plane) and 3(volume).

Assuming that all intrusion pores are composed of capillaries, the Washburn equation can be used to describe the relationship between pore the diameter  $d_p$  and the intrusion pressure  $P$  [37]:

$$d_p = \frac{-4\gamma \cos \theta}{P} \quad (10)$$

Combining Eqs. (9) and (10), provides the following relation between  $S$  and  $P$ :

$$\log S \propto (D_p - 2) \log P \quad (11)$$

The relation between  $\log S$  versus  $\log P$  is shown in Fig. 11. The pores fractal dimension  $D_p$  is calculated from the slope of the curve  $\log S$  versus  $\log P$ .

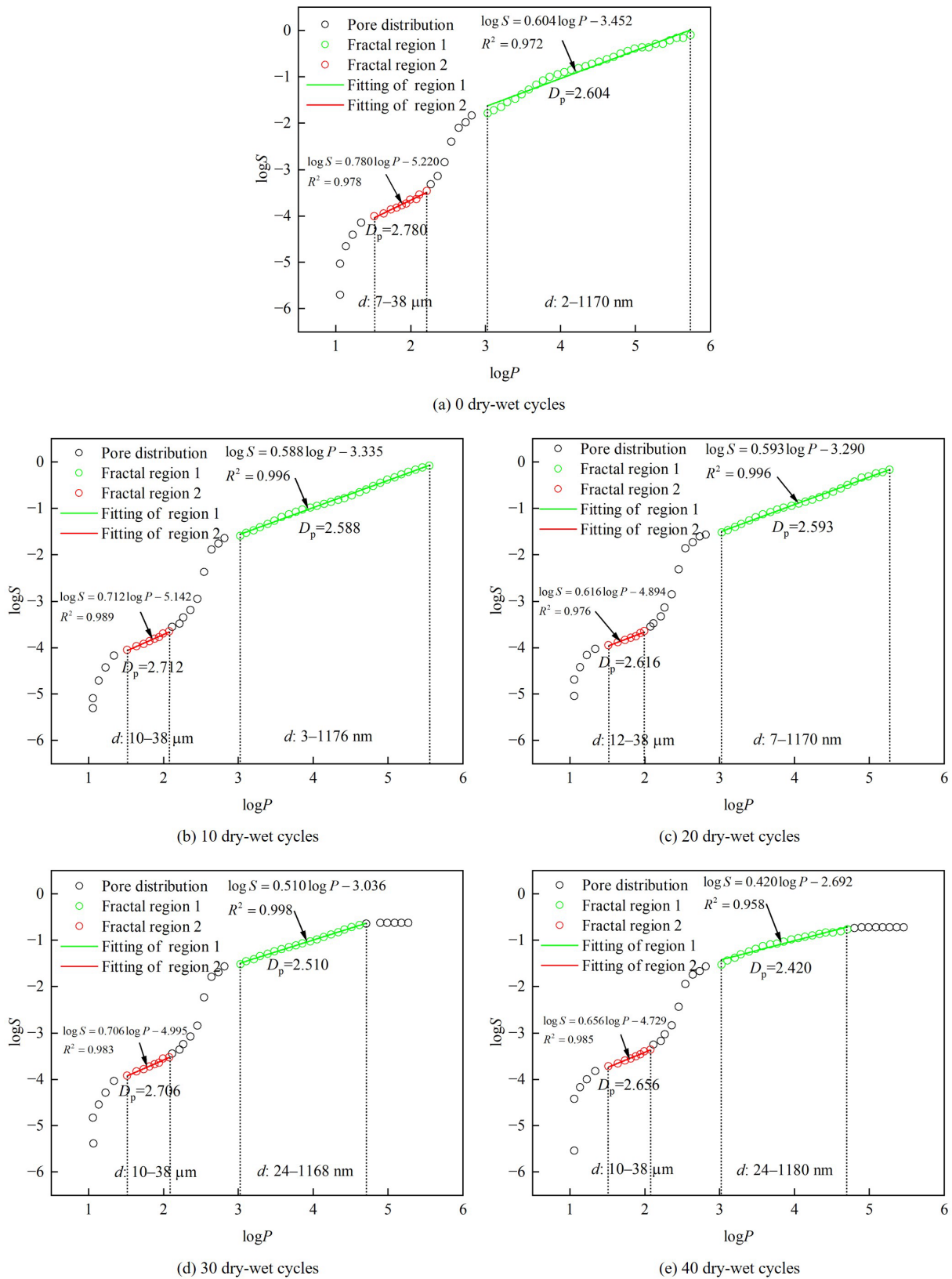


**Fig. 11.** The effect of the dry-wet cycles on the curve  $\log S$  versus  $\log P$ .

Fig. 11 shows that there are two fractal regions according to the Neimark model; the slopes of the remaining regions are beyond the Neimark dimension range. The fractal region 1 corresponds to the micro- and mesoscale pores smaller than 1200 nm, while the fractal region 2 corresponds to the macropores smaller than 40  $\mu\text{m}$ . The

distributions of micro-, meso-, and macro-pores are multi-fractal, or scale-dependent fractal. The fractal dimensions of macropores are consistently larger than those of micro- and meso-pores, indicating a significant disparity in the size distribution between micro-mesopores and macropores. This disparity remains unaffected by the cyclic dry-wet process.

Fig. 12 shows the effect of dry-wet cycles on the fractal dimension of micro-mesopores and macropores. It can be seen that  $D_p$  of micro-mesopores is nearly constant during the first 20 cycles and then drops from 2.593 after 20 dry-wet cycles to 2.420 after 40 dry-wet cycles, while  $D_p$  of macropores decreases from 2.780 at 0 dry-wet cycle to 2.616 after 20 dry-wet cycles, increasing between 20 and 30 dry-wet cycles, and decreasing again between 30 and 40 cycles to a final value of 2.650. This implies that the pore uniformity across different scales changes significantly during the dry-wet cycle process. With progress of dry-wet cycles, the size uniformity of macropores first rises and then fluctuates, while the size uniformity of micro-mesopores is initially constant and subsequently increases.

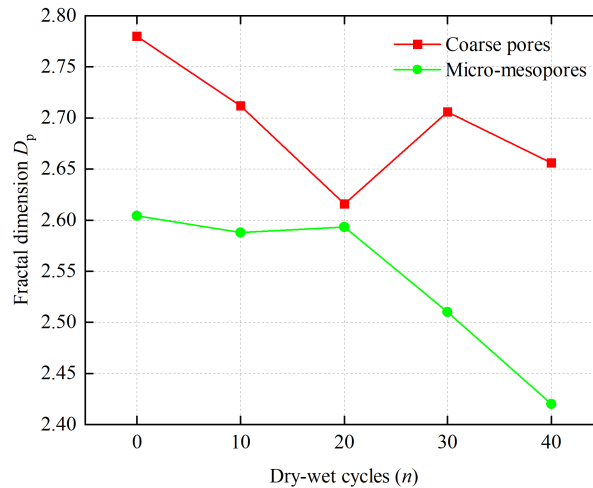


Fig. 12. The effect of the dry-wet cycles on the pore's fractal dimension.

Considering the variation of fractal dimension in different pore scales, it can be speculated that the dissolution and precipitation of minerals play an important role in the pore space evolution. During the first 20 dry-wet cycles, the soluble coarse-grained minerals such as feldspar, which account for a larger proportion, are the first to dissolve and precipitate. The macropores around these minerals undergo expansion or restructuring which increase the uniformity of the macropores. Simultaneously, due to the limitation of pore size and seepage channels, the soluble micro-nano minerals have little contact with water and the uniformity of the surrounding micro-mesopores does not change. During the next 20 dry-wet cycles, the pore space and seepage channels expand rapidly so that the soluble micro-nano clay minerals quickly dissolve, increasing the size uniformity of the surrounding micro-mesopores. With the reduction of soluble minerals, the macropores expose larger surface areas and the pore space becomes more susceptible to collapse, resulting in fluctuating uniformity of macropore sizes. In addition, the effect of temperature variation involved in dry-wet cycles on micro-nano minerals is noticeable. Esther et al. determined the mineral mobilisation from 25 to 150 °C, and found that the kaolinite was more easily activated and ionized with the increase of temperature, which promoted particle aggregation and bridging in the pore throats and contributed to the permeability reduction in sandstone samples [38]. This phenomenon has a further influence on the characteristics of mineral morphology and crack expansion in hydrodynamic damage process of the dry-wet cycles [39,40].

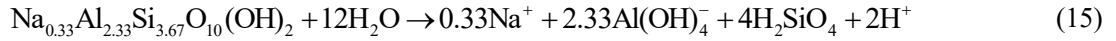
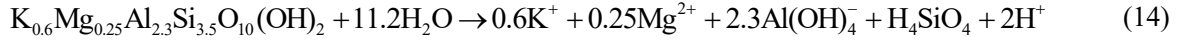
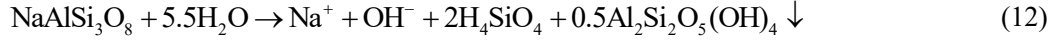
### 3.5. Microstructure characteristics

The current understanding of rocks' behaviour during dry-wet cycles is that the deterioration is due to the cycles' action on pores and cracks [41]. However, the pore structure analysis in the previous section indicates that the effect of the cyclic dry-wet process on sandstone is more complex. Micromorphology study of samples in different dry-wet cycles is necessary to further understand the deterioration mechanism. Fig. 13 shows BSE images of sandstone samples after different dry-wet cycles, which are used to investigate the destruction of mesoscopic minerals (<500  $\mu\text{m}$ ). The samples of sandstone used for BSE imaging under the same condition have been traversed to observe at least five positions to eliminate local limitations, and the observation process has been carried out in the form of layer-by-layer magnification to capture more information.

Fig. 13a shows the mineral junctions with magnification of 2000; scale bars are 50  $\mu\text{m}$ . At 0 dry-wet cycle, the mineral grains have rough boundaries and strong cementation. A few pores located at grain boundaries are observed. With increasing dry-wet cycles, the rough boundaries gradually disappear leaving more regularly shaped grains. After 20 dry-wet cycles, clear transgranular and intergranular (broken grain boundaries) cracks are visible, and the pores at grain boundaries rapidly develop. As the dry-wet cycles continue, the grain shapes change and the microstructure exhibits residual grain bonding (intergranular crack bridges), grain dissolution, shrink boundaries,

etc. After 40 dry-wet cycles, the grain structure is significantly damaged and different minerals blend into each other with clear transgranular and intergranular cracks.

Fig. 13b shows the particle distribution with magnification of 200; scale bars are 500 nm. The mineral particles become more distinct with increasing dry-wet cycles. To explain this observation, Table 5 gives the percentage of element mass. It can be seen that the mass fractions of Al, Mg, Na, and Ca continuously decrease during the cyclic dry-wet process, which is due to hydrolysis of the feldspars and clay mineral [42,43]. The hydrolysis is described by the equations:



The hydrolysed precipitates are more likely to form around feldspar minerals. At the same time, the mass fraction of Si increases with the dry-wet cycles, suggesting that the cyclic dry-wet process has little effect on siliceous skeleton minerals. It can be concluded that the fine-grained clay minerals are eroded during the dry-wet cycles, while the skeleton minerals like quartz are less affected, resulting in the overall weakened cementation of sandstone particles.

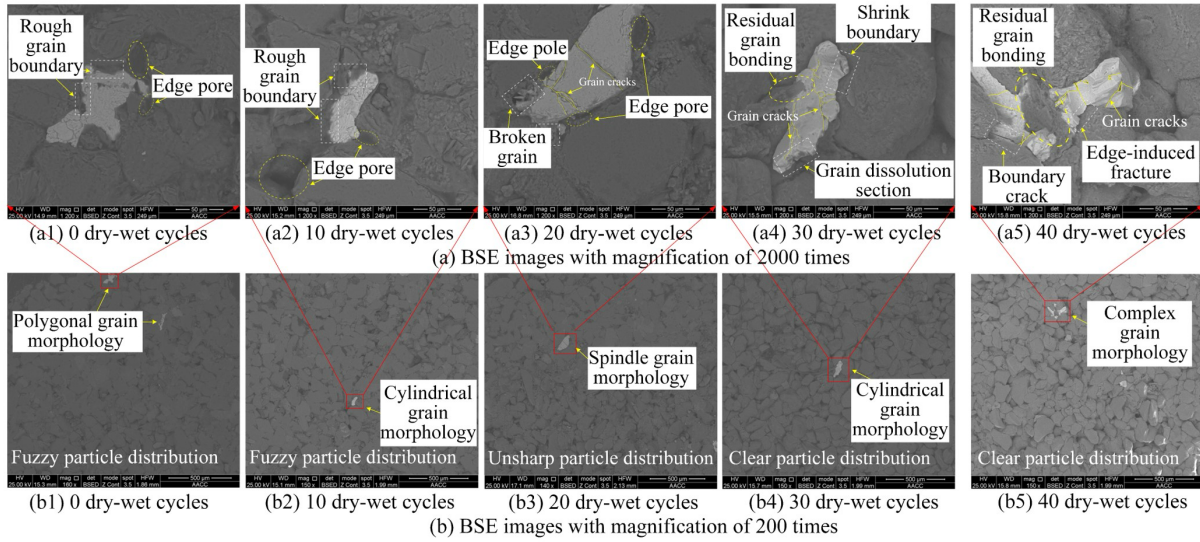
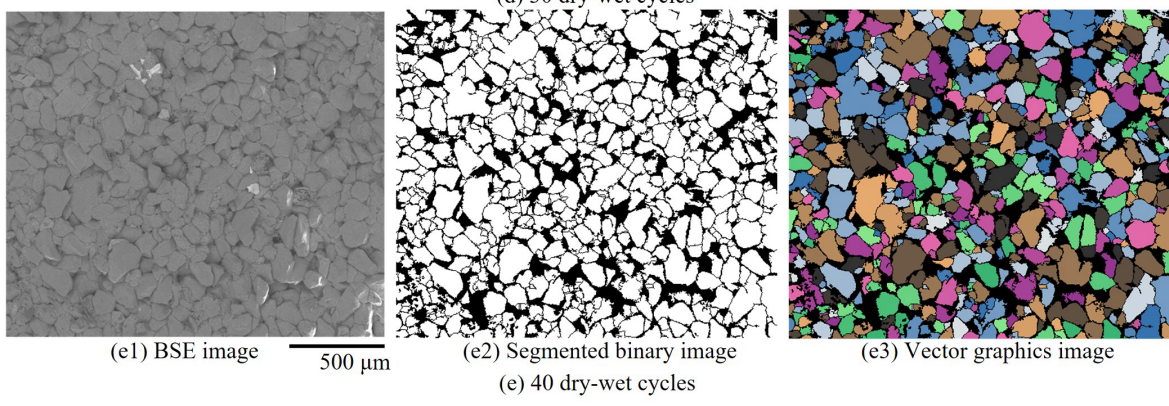
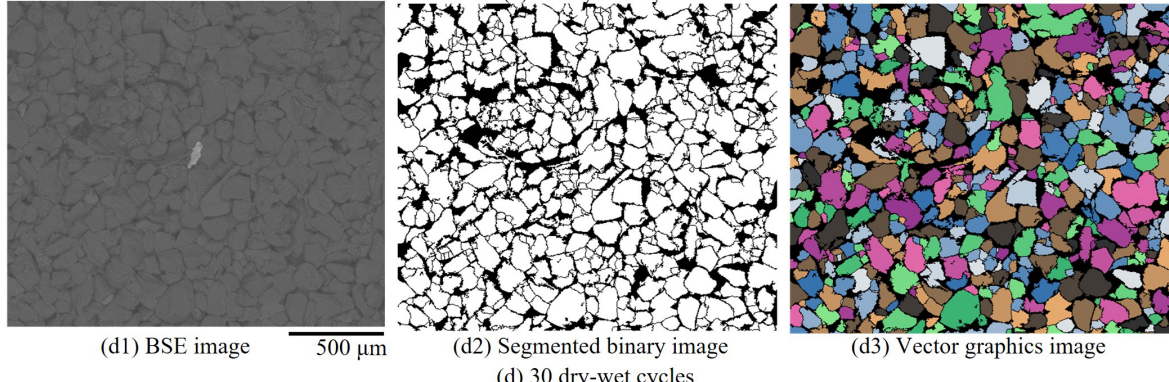
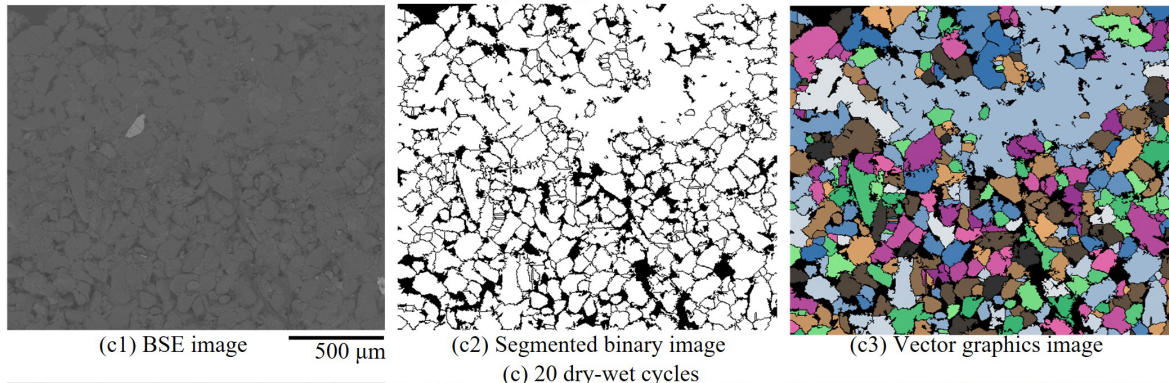
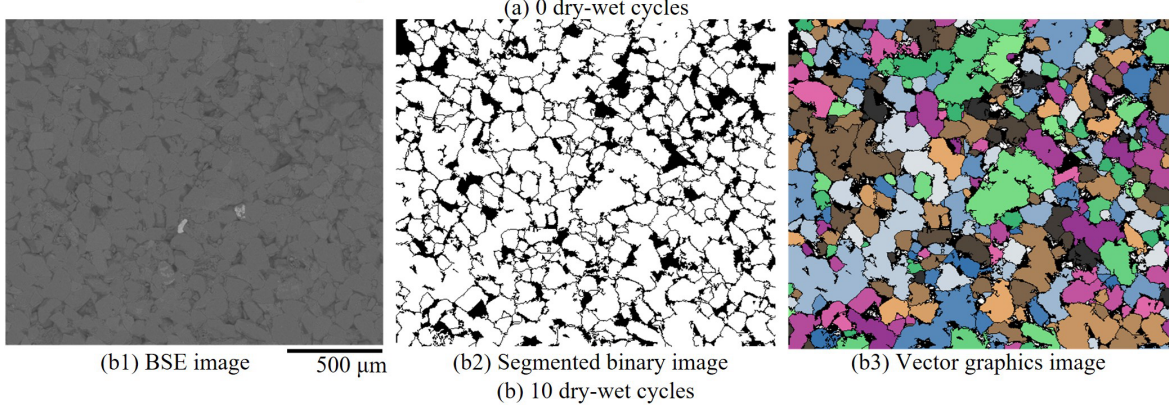
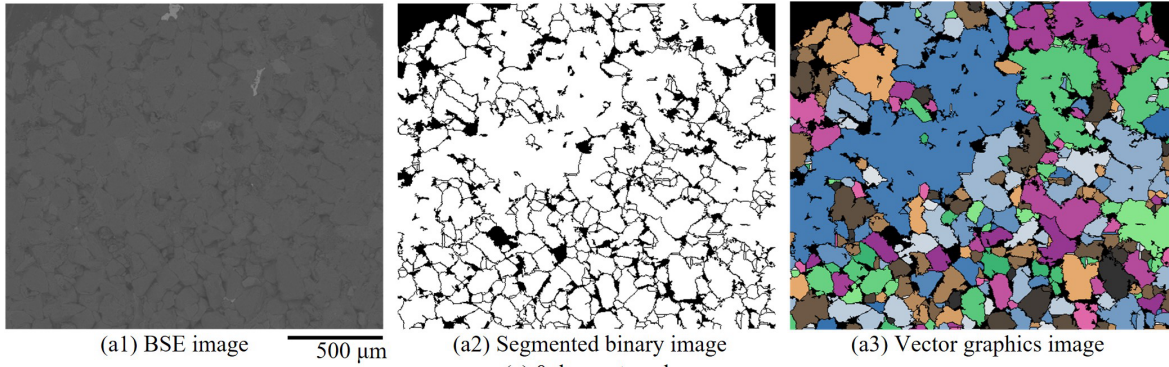


**Fig. 13.** Micromorphology based on BSE images.

**Table 5** The percentage of element mass under different dry-wet cycles.

Dry-wet cycles (n)	Ca (%)	K (%)	Si (%)	Al (%)	Mg (%)	Na (%)	O (%)	C (%)	H (%)
0	5.1	3.2	28.3	10.0	0.4	2.7	48.8	1.4	0.1
10	4.5	3.4	29.8	9.2	0.4	2.6	48.9	1.1	0.1
20	4.1	3.5	30.0	8.4	0.2	2.2	50.3	1.2	0.1
30	3.9	3.4	31.5	7.6	0.1	2.1	50.0	1.3	0.1
40	3.5	3.2	33.0	7.5	0.1	2.0	49.3	1.3	0.1

To quantify the effect of dry-wet cycles on the mineral particle distribution of sandstone, the digital image recognition software Pores/particles and Cracks Analysis System (PCAS) is used [44]. Fig. 14 illustrates the process of threshold segmentation and the fitting for BSE images after different dry-wet cycles. Fig. 15 shows the effect of dry-wet cycles on the statistical parameters of particle distribution. The results show that the total particle area and the average particle area steadily decrease with increasing dry-wet cycles. The average perimeter of mineral particles first increases and then keeps decreasing with increasing dry-wet cycles. This means that during the early stage of dry-wet cycles, a significant number of large particles are disintegrated into multiple small particles. Although the particle number increases rapidly after 10 dry-wet cycles, the reduction of particle size caused by dry-wet cycles is still dominant, resulting in a continuous decrease in average perimeter. Correspondingly, the fractal dimension of particles continuously decreases during the cyclic dry-wet process, indicating that the uniformity of mineral particles steadily increases. Probability entropy represents the degree of certainty in particle distribution, and its value gradually approaches 1, indicating that the distribution of mineral particles becomes homogeneous with the increase of dry-wet cycles.



(a) 0 dry-wet cycles  
(b) 10 dry-wet cycles  
(c) 20 dry-wet cycles  
(d) 30 dry-wet cycles  
(e) 40 dry-wet cycles

**Fig. 14.** Images segmentation with PCAS after different dry-wet cycles.

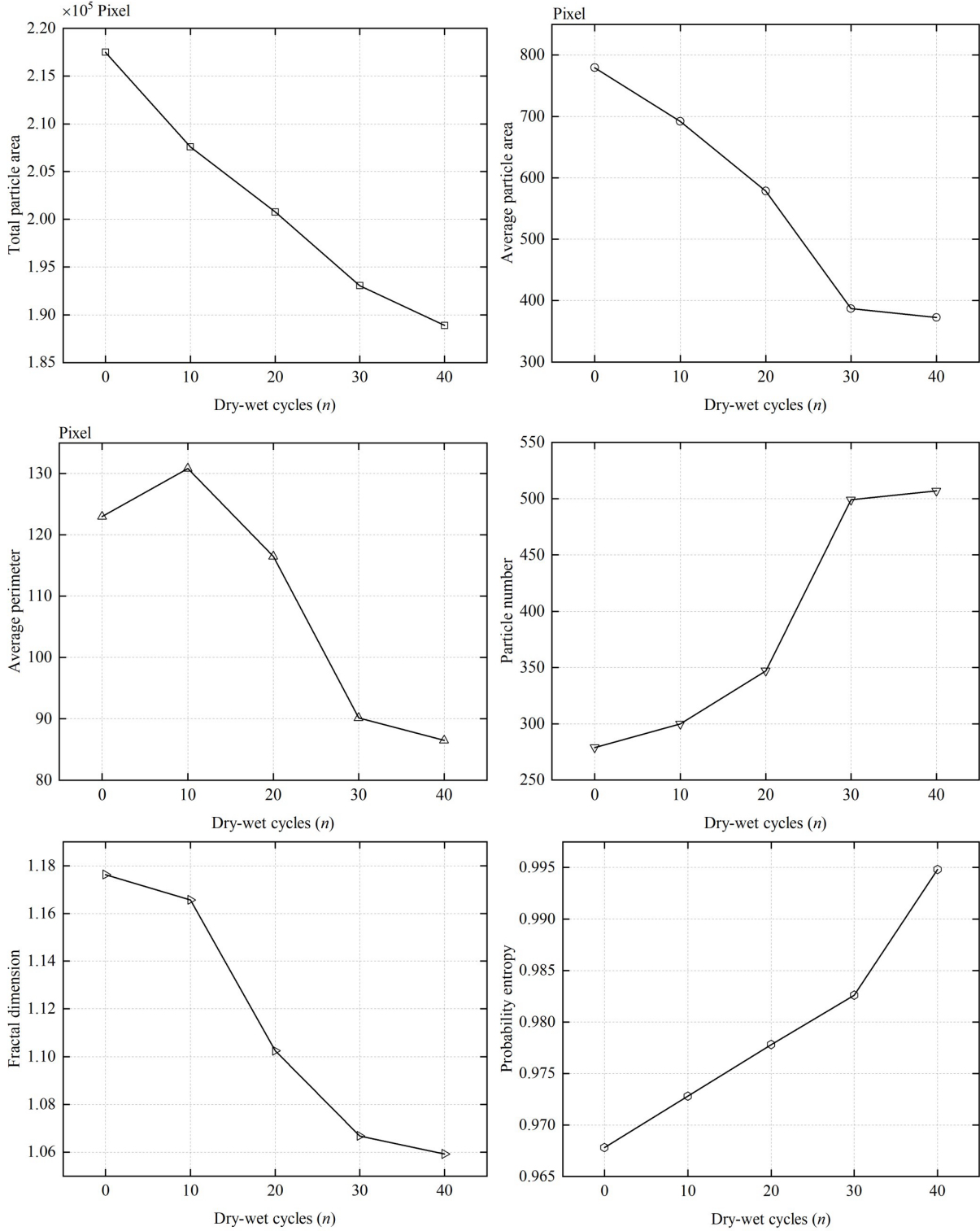


**Fig. 15.** The effect of dry-wet cycles on the statistical parameters of particle distribution.

## 4. FEM-DEM simulation of dry-wet damaged sandstone under dynamic load

### 4.1. Methodology

In SHPB impact test, the striker and the bars are made of steels with high yield strengths and elastic moduli. For simulating the propagation of waves through these parts, it is sufficient to model them as continuous media. The sandstone specimen is a typical porous medium that undergoes both elastic deformation and irreversible fracture under dynamic loading. For simulating fracture without prescribing specific crack locations, it is appropriate to model the sandstone as a collection of discrete particles. Therefore, a coupled continuous-discrete method is required



for the numerical simulation of dynamic impact on sandstone. The approach adopted in this work is illustrated in Fig. 16; the subfigures are discussed in the following paragraphs.

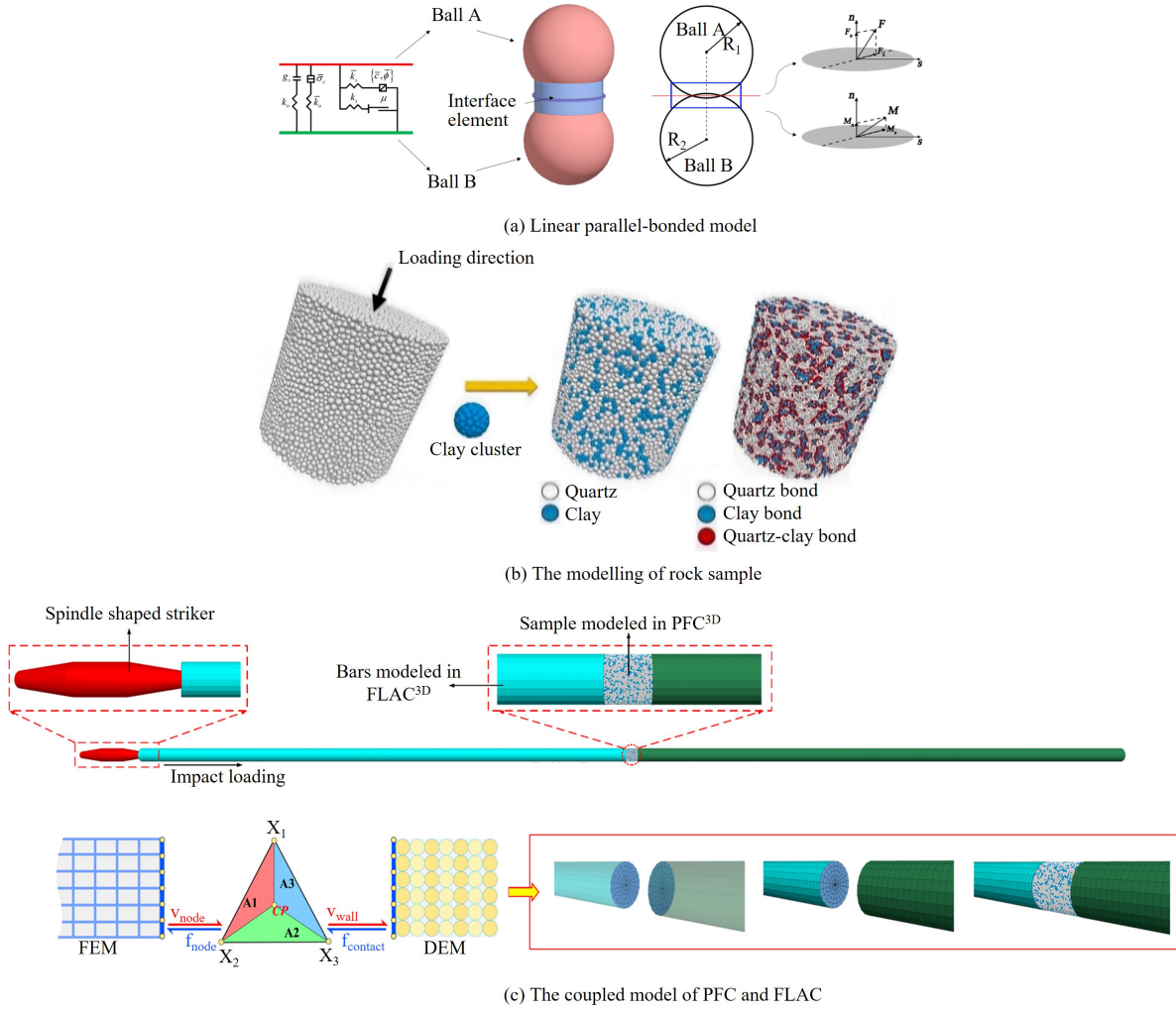


**Fig. 16.** The numerical methodology of SHPB impact test.

The sandstone samples are modelled using the Particle Flow Code (PFC) software [45]. The mineral components are characterized through the built-in cluster body module. The sample modelling considers two typical types of minerals – quartz and clay – to simplify the management of micro-parameters. During the simulation process, the sample porosity, the mineral proportion, and the bond strength of mineral clusters are adjusted by referring to the quantified results of damage characterization in the previous sections. The contact behaviour of mineral particles is determined by the real rock failure features. To this end, it is considered that the cementations are widely distributed among the rock particles and the bonding matrix so that the cohesive strength and internal friction are dominant. The bonded-particle model (BPM) proposed by Potyondy and Cundall et al. [46] is capable of simulating various mechanical behaviors of rock materials, including elasticity, fracture, dilation, softening, and hysteresis. The parallel-bond model is a type of BPM, involving a normal bonding component and a parallel bonding component, as shown in Fig. 16a. The normal bonding component can provide a linear elastic force and a damping force as feedback of compressive stress, while the parallel bonding component can bear the tensile, compressive stress and force moment within the limit of the bond gap. In the process of rock brittle fracture, the elastic force and damping force of the normal bonding component are updated in each calculating step. The parallel bonding component will first decompose the external stress into normal and tangential force as well as the moment into torque and bending moment, and then update elastically within the defined bonding gap range. When the bonding units are broken, the action of the parallel bonding component disappears, and the BPM reverts to a simple Newtonian model that contains only the normal bonding component. The specific force-displacement laws are:

$$\begin{cases} F_c = F_1 + F_d + \bar{F} \\ M_c = \bar{M} \end{cases} \quad (16)$$

where  $F_c$  is the contact force;  $F_1$  the linear force;  $F_d$  the dashpot force;  $\bar{F}$  the parallel-bond force;  $M_c$  the contact moment; and  $\bar{M}$  the parallel-bond moment. The updating rules are:

$$\begin{cases} \bar{\mathbf{F}} = -F_n \hat{\mathbf{n}}_c + \bar{\mathbf{F}}_s \\ \bar{\mathbf{M}} = \bar{M}_t \hat{\mathbf{n}}_c + \bar{\mathbf{M}}_b \end{cases} \quad (17)$$

where  $\bar{\mathbf{F}}$  is the contact force in next timestep;  $F_n$  the normal force;  $\bar{\mathbf{F}}_s$  the shear force;  $\bar{\mathbf{M}}$  the contact moment in next timestep;  $\bar{M}_t$  the torque moment;  $\bar{\mathbf{M}}_b$  the bending moment; and  $\hat{\mathbf{n}}_c$  the normal vector of contact surface.

A parametric study with a set of micro-bonding parameters was performed to determine the values describing effectively the mechanical behaviour of sandstone under uniaxial loading. Specifically, it includes three key steps: (1) stress response calibration of sample model; (2) peak strength calibration of sample model; and (3) brittleness and plasticity calibration of sample model. According to this sequence, the contact stiffness, Young modulus, bond strength, friction coefficient, radius parameters, etc. were tested by the control variable method. When the stress-strain curve obtained from FEM-DEM simulation is consistent with the laboratory test, the micro-bonding parameters are considered reasonable. The validated micro-bonding parameters are given in Table 6. The linear BPM with these parameters was used for the contacts between rock particles, and the simple Newtonian model was adopted for the contacts between rock and boundaries.

For modelling the striker and the bars, the built-in module of Fast Lagrange Analysis of Continua (FLAC) was used. The striker was modelled as spindle-shaped to ensure a quick stress equilibrium of rock samples [47]. The elastic modulus was set at 210 GPa and the Poisson's ratio at 0.25 for all steel parts. As shown in Fig. 16c, the grid walls in PFC were placed at the contact surfaces between continuous bar elements and discrete rock particles. The coordinates, velocities, and forces of each node were updated with the barycentric interpolation method. This ensures consistent coupling of the continuous and the discrete models.

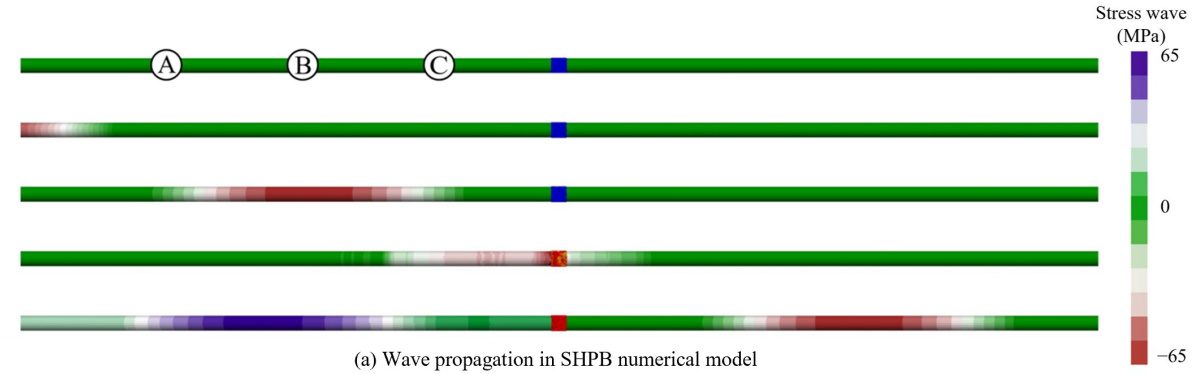
**Table 6** Micro-parameters of sandstone model

	Micro-parameter	Quartz	Clay	Quartz-Clay
Basic elements	Particle density (kg/m <sup>3</sup> )	2700	1500	
	Damp factor	0.8	0.6	
	Minimum particle radius (mm)	0.6	0.2	
	The ratio of maximum to minimum particle radius	1.8	1.6	
	Stiffness ratio	2.7	2.5	1.5
	Friction angle (°)	20.0	18.0	25.0
0 dry-wet cycle	Porosity (%)	20.4		
	Volume composite (%)	73.1	26.9	
	Cohesion strength (MPa)	80.0	60.0	40.0
	Tension strength (MPa)	40.0	30.0	20.0
	Young modulus (GPa)	10.0	5.0	2.0
10 dry-wet cycles	Porosity (%)	24.2		
	Volume composite (%)	75.2	24.8	
	Cohesion strength (MPa)	58.0	44.0	30.0
	Tension strength (MPa)	29.0	22.0	15.0
	Young modulus (GPa)	7.5	3.6	1.2
20 dry-wet cycles	Porosity (%)	28.5		
	Volume composite (%)	79.6	20.4	
	Cohesion strength (MPa)	52.0	40.0	26.0
	Tension strength (MPa)	26.0	20.0	13.0
	Young modulus (GPa)	4.5	1.2	0.8
30 dry-wet cycles	Porosity (%)	31.6		
	Volume composite (%)	87.2	12.8	
	Cohesion strength (MPa)	48.0	36.0	24.0
	Tension strength (MPa)	24.0	18.0	12.0
	Young modulus (GPa)	3.2	0.6	0.5
40 dry-wet cycles	Porosity (%)	36.8		
	Volume composite (%)	87.6	12.4	
	Cohesion strength (MPa)	46.0	32.0	20.0
	Tension strength (MPa)	23.0	16.0	10.0
	Young modulus (GPa)	1.4	0.5	0.4

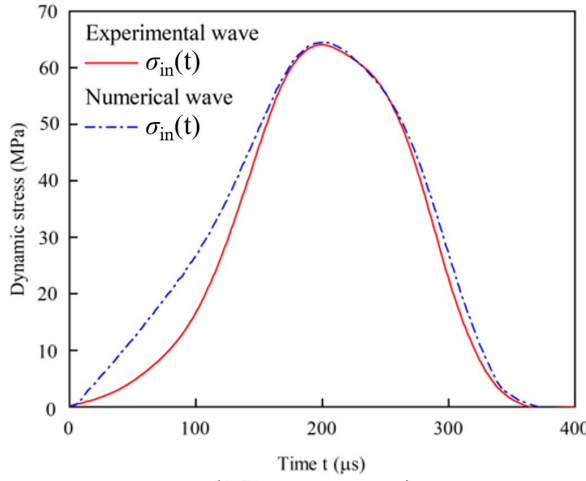
#### 4.2. Verification and validation of the numerical model

Numerical simulations of the uniaxial impact tests were performed. Fig. 17a presents the stress time history of incident bar after impact loading. The compressive stress wave propagates along the  $x$ -direction. When it reaches the contact surface, a fraction of the wave energy is transmitted to the sample as a compressive pulse, and the remaining energy is reflected as a tensile pulse. The stress time history at the measuring points is presented in Fig. 17b. The stress wave amplitudes in  $x$ -direction at all points are identical, suggesting negligible dispersion in  $y$ - and  $z$ -direction. Thus, the SHPB numerical model satisfies the requirement for one-dimensional stress wave propagation. Additionally, the three-wave method is employed to perform the dynamic stress equilibrium of the sample. As shown

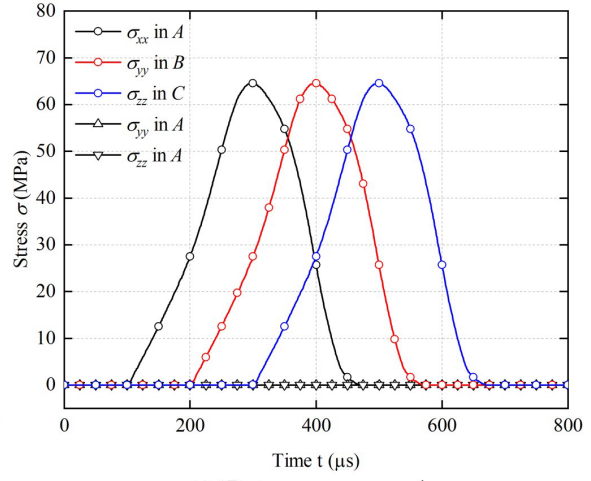
in Fig. 17c, the sum of the compressive stress wave and tensile stress wave on incident bar equals the compressive stress wave on transmitted bar, indicating that the sample model meets the dynamic stress equilibrium condition during the impact loading. As listed in Table 6, multiple SHPB numerical tests were conducted on the calibrated sample models, and the comparison with experimental stress-strain curves is shown in Fig. 17d. Table 7 gives the DCS value and peak strain value in each dry-wet cycle, and the comparison validates the SHPB numerical model.



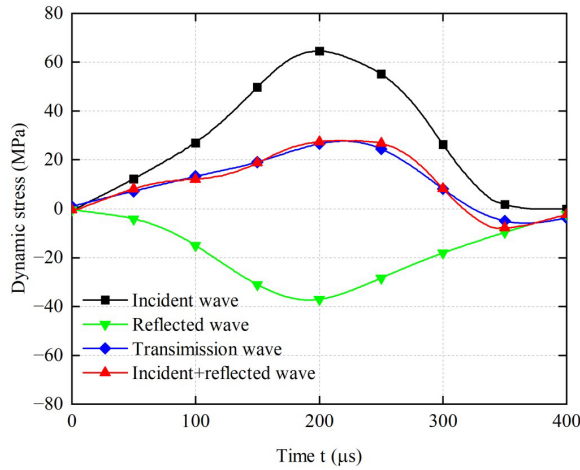
(a) Wave propagation in SHPB numerical model



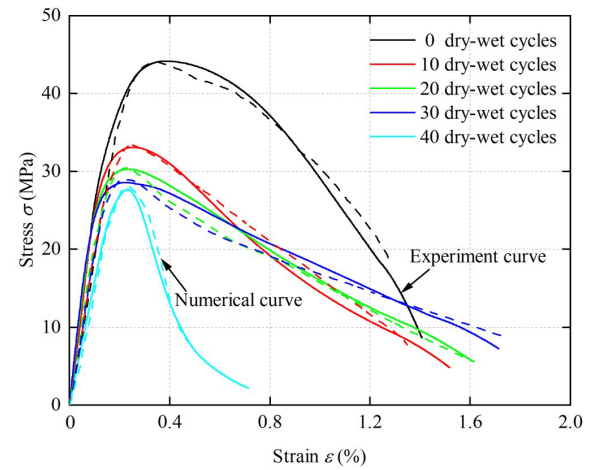
(b) Stress wave comparison



(c) 1D stress wave propagation



(d) Dynamic stress equilibrium



(e) Strain-stress comparison

**Fig. 17.** Validation of SHPB numerical simulation.

**Table 7** The comparison of experimental results and simulated results

Dry-wet cycles	Experimental value		Simulated value		
	(n)	DCS (MPa)	Peak strain (%)	DCS (MPa)	Peak strain (%)
0		44.12	0.38	44.06	0.35
10		33.09	0.25	33.34	0.25
20		30.27	0.23	30.42	0.22
30		28.58	0.22	28.94	0.23
40		26.74	0.23	27.01	0.24

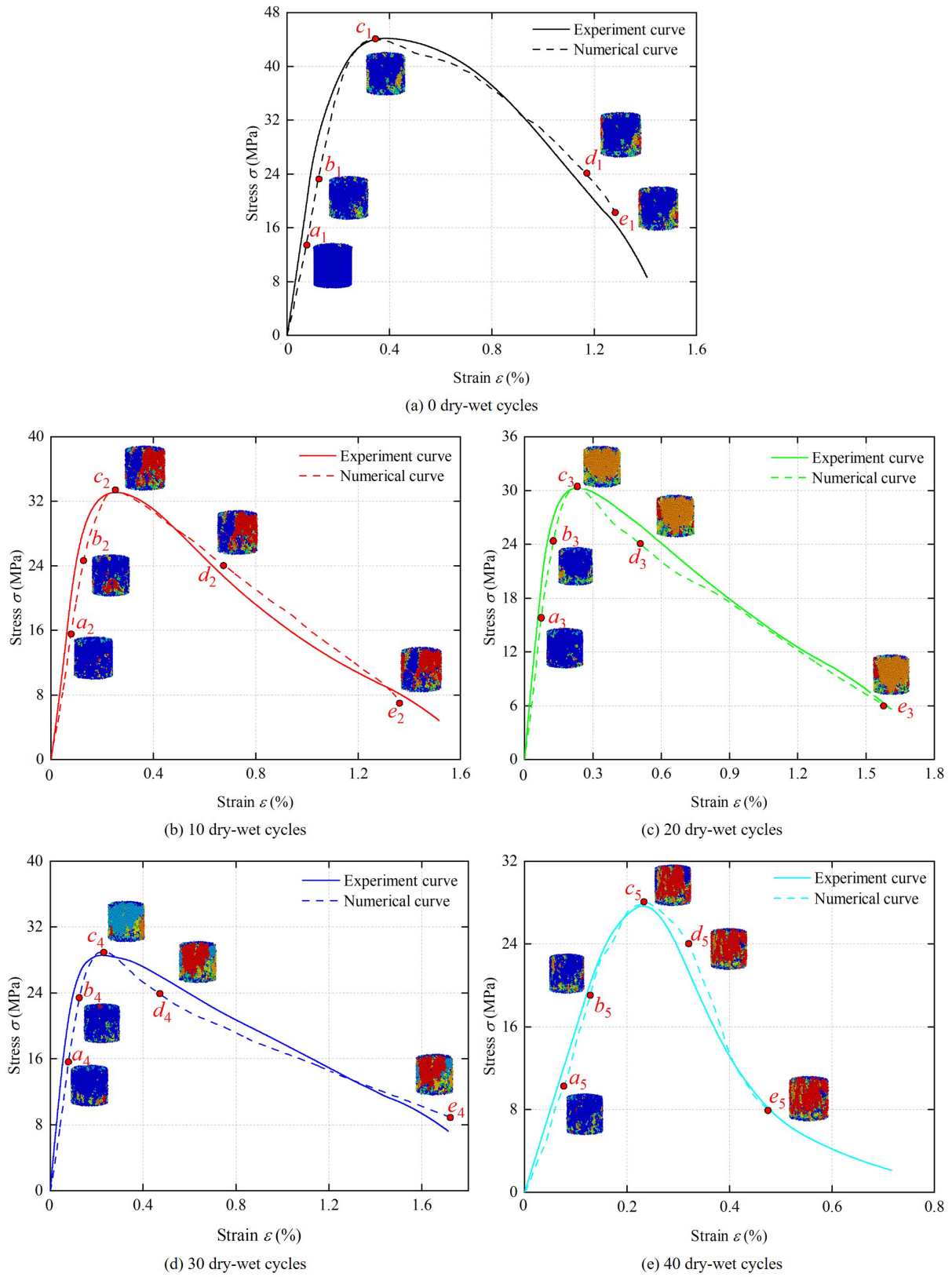
## 5. Numerical results and discussion

### 5.1. Damage and failure characteristics

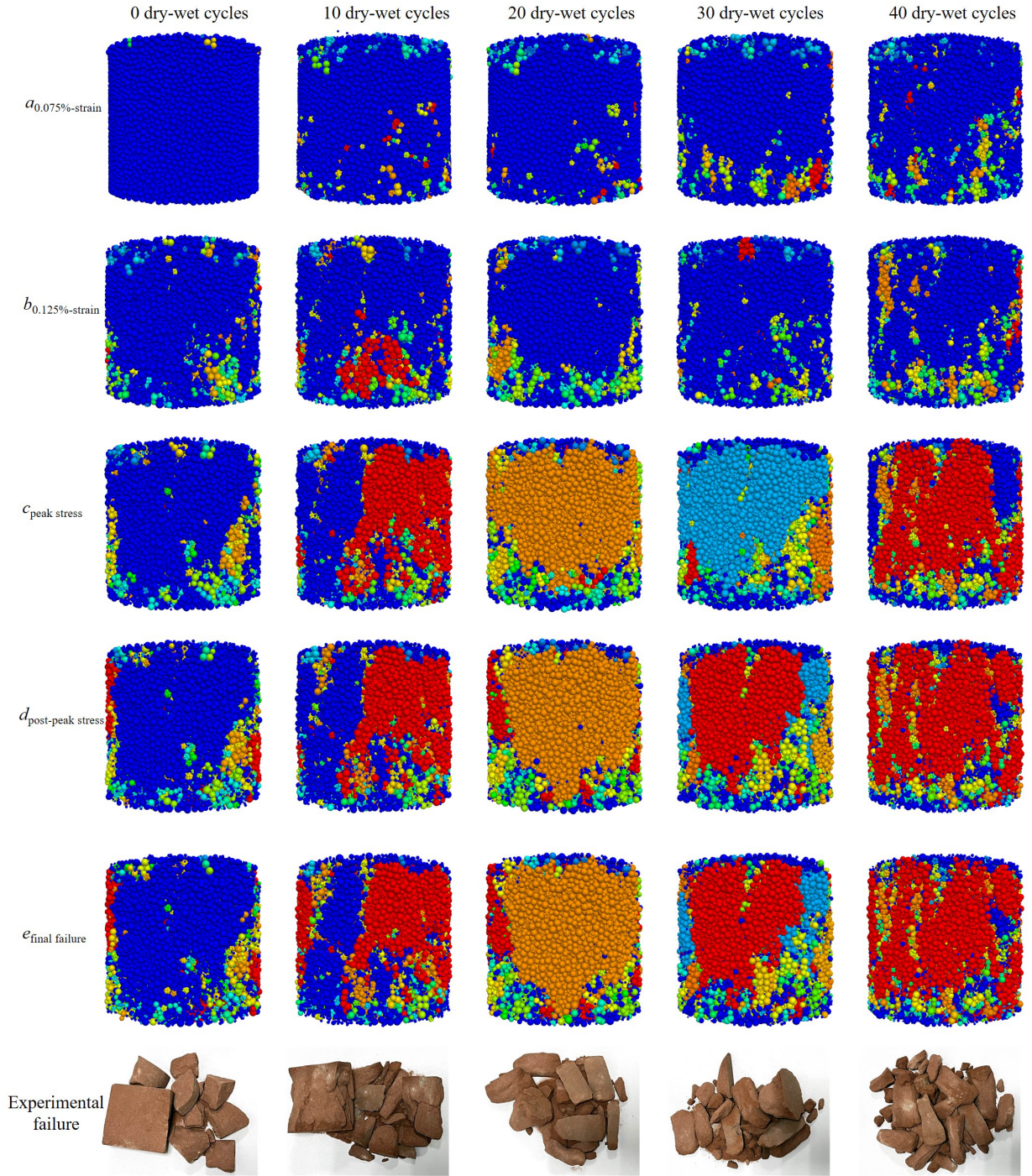
The dynamic strain-stress behaviour and the failure characteristics of sandstone in different dry-wet cycles calculated with the numerical model are shown in Fig. 18a–e. To illustrate the process of rock damage and failure, five points are selected on the strain-stress curves: *A* at 0.075% strain (pre-peak), *B* at 0.125% strain (pre-peak), *C* at peak stress, *D* at 24 MPa stress (post-peak), and *E* at failure. It can be observed from Fig. 18a–e that the pre-peak stiffness of the numerical model (at points *A* and *B*) is lower than the experimental stiffness. This is due to the particle flow properties of the rock model. Apart from this, the simulated strain-stress behaviour is in very good agreement with the experimentally measured behaviour. This provides confidence that the model captures the effect of dry-wet cycles on the progressive failure well.

Fig. 19 compares typically calculated damage patterns in sandstone after different dry-wet cycles. Damage accumulated between points *A* and *B*, within 0.05% strain increment, and first localisations of damage can be observed at point *B*. The accumulation and localisation of damage is enhanced by increasing dry-wet cycles. The damage is spreading widely between points *B* and *C*, and at the peak stress the future fragmentation of the rock takes shape. At point *C*, the difference in the damage patterns between the different dry-wet cycles is maximal. At the post-peak points *D* and *E*, the damage patterns are similar, apart from the observation that more dry-wet cycles lead to larger fragmentation, i.e., smaller fragments at point *E*.

The results suggest that in the pre-peak stage, the failure patterns are governed by the strain, and that the dry-wet cycles primarily contribute to increased fragmentation at the peak stress. The failure patterns remain nearly constant after the peak stress which is confirmed by the experimental failure patterns. It can be concluded that the dry-wet cycles affect the entire process of dynamic failure. Point *C*, serving as a transition point, best illustrates the impact of dry-wet cycles.



**Fig. 18.** The strain-stress curve comparison and the progressive failure process.



**Fig. 19.** The effect of the dry-wet cycles on the dynamic failure progress.

## 5.2. Energy partitions

In underground engineering, the energy absorption characteristics of rock layers serve as a crucial indicator for the influence of dynamic loading and cyclic water erosion environment. In SHPB tests, the energy absorbed by the samples is calculated as the difference between the elastic energy of the incident wave and the energies of the transmitted and reflected waves [48]. However, the energy absorbed by the samples is transformed into heat energy due to friction, kinetic energy of fragments, fracture energy due to new surface generation, etc. [49]. These forms of energy are difficult to measure with the existing equipment, but the numerical method provides a feasible approach to differentiate between forms of energy. There are three types of energy recorded during the impact process: (1) kinetic energy due to the motion of particles,  $E_{\text{kinetic}}$ ; (2) strain energy stored in bonds and contacts of particles,  $E_{\text{strain}}$ ; and (3) dissipated energy by particles slip, friction or fractures formation, etc.,  $E_{\text{dissipated}}$ . Since the parameters of the numerical model do not change during impact, the energy absorbed by the specimen is given by:

$$W_{\text{absorption}} = E_{\text{kinetic}} + E_{\text{strain}} + E_{\text{dissipated}} \quad (18)$$

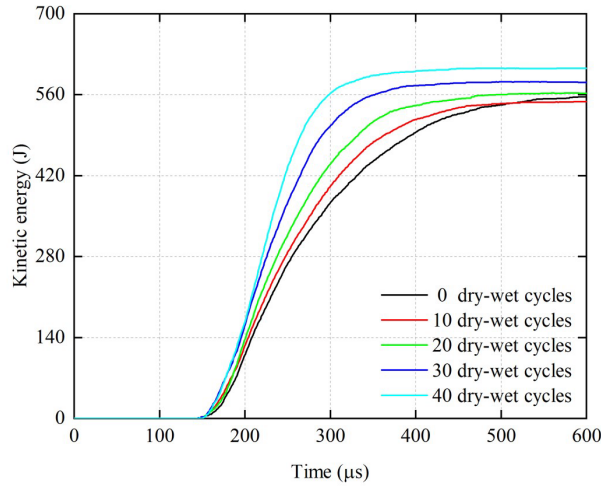
$$E_{\text{kinetic}} = \frac{1}{2} m_i v_i^2, \text{ for } i = 1L \ n \quad (19)$$

$$E_{\text{strain}} = \frac{1}{2} \left( \frac{(\mathbf{F}_n^1)^2}{k_n} + \frac{\|\mathbf{F}_s^1\|^2}{k_s} + \frac{\bar{F}_n^2}{\bar{k}_n \bar{A}} + \frac{\|\bar{\mathbf{F}}_s\|^2}{\bar{k}_s \bar{A}} + \frac{\bar{M}_t^2}{\bar{k}_s \bar{J}} + \frac{\|\bar{\mathbf{M}}_b\|^2}{\bar{k}_n \bar{I}} \right) \quad (20)$$

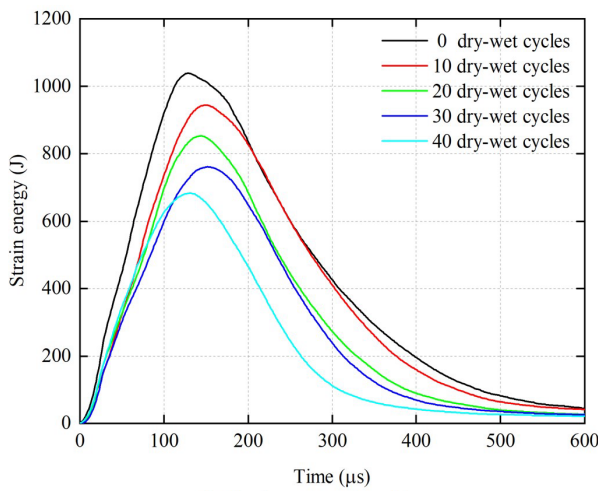
$$E_{\text{dissipated}} = \mathbf{F}_c \cdot (\Delta\delta_n + \Delta\delta_s) \quad (21)$$

where  $W_{\text{absorption}}$  is the total energy absorbed by sandstone model,  $m_i$  and  $v_i$  are the mass and velocity of the  $i$ -th particle element, respectively;  $\mathbf{F}_n^1$  and  $\mathbf{F}_s^1$  the normal and shear forces of linear bonding component, respectively;  $k_n$  and  $k_s$  the normal and shear stiffness of linear bonding component, respectively;  $\bar{F}_n$  and  $\bar{F}_s$  the normal and shear forces of parallel bonding component, respectively;  $\bar{k}_n$  and  $\bar{k}_s$  the normal and shear stiffness of parallel bonding component, respectively;  $\bar{A}$  the cross-sectional area;  $\bar{I}$  the moment of inertia of the parallel bonding component,  $\bar{J}$  the polar moment of inertia of parallel bonding component;  $\bar{M}_t$  and  $\bar{M}_b$  the torque and bending moment of parallel bonding component, respectively;  $\mathbf{F}_c$  the contact force; and  $\Delta\delta_n$  and  $\Delta\delta_s$  the normal and tangential relative displacement recorded by the contact dissipative component, respectively.

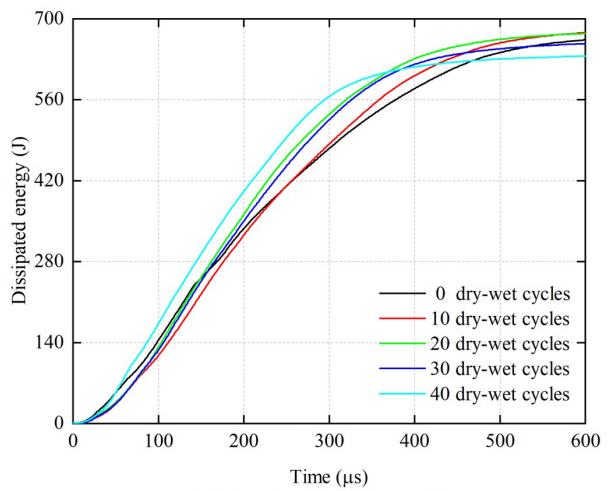
Fig. 20a–c shows the effect of the dry-wet cycles on the time-history of the three energy forms. The figure shows that most of  $W_{\text{absorption}}$  is initially stored as strain energy, while the kinetic energy remains at zero as the rock is still intact. When the peak of strain energy is approached, the cement and contact strength of the rock particles reach their limits, leading to local ruptures. From this moment, the strain energy is gradually released and most of  $W_{\text{absorption}}$  is consumed by rapid growth of kinetic energy and dissipated energy. The dry-wet cycles mainly affect the conversion efficiency of this process. In Fig. 20a, the rate of kinetic energy increases with the dry-wet cycles, and the samples after 40 dry-wet cycles have the largest peak. In Fig. 20b, the peak of strain energy decreases with the dry-wet cycles. It is difficult to establish a consistent effect of dry-wet cycles on the dissipated energy; nevertheless, it is clear that the dissipated energy after 40 dry-wet cycles has the highest growth rate and the lowest peak value. In summary, the time-histories of different energies indicate that the samples at 0 dry-wet cycle show the best efficiency of absorbing energy as stored strain energy with the highest peak value. With increasing dry-wet cycles, the absorption in the form of strain energy is significantly reduced due to the deterioration of bonds and contacts. Consequently, the specimens become more fragile, leading to a continuous increase in both the peak value and growth rate of kinetic energy. After 40 dry-wet cycles, the clay mineral content is significantly lower than that of the high-strength quartz. As a result, the load-bearing capacity of the rock skeleton structure is slightly enhanced, leading to a minor increase in the growth rate of strain energy. However, the majority of absorbed energy is still in the form of kinetic and dissipated energy, resulting in an overall poorest dynamic performance.



(a) Kinetic energy time history



(b) Strain energy time history



(c) Dissipated energy time history

**Fig. 20.** The effect of the dry-wet cycles on the loading time-energy curves.

Fig. 21a–c illustrates the effect of dry-wet cycles on the three energies as functions of the applied strain. Fig. 21a shows that the strain levels at which kinetic energy is first recorded decrease with the increase of dry-wet cycles; the reductions between 0 to 10 and 30 to 40 dry-wet cycles are most apparent. Fig. 21b shows that the slopes of strain-strain energy curves increase with the dry-wet cycles, while the peak values decrease. This indicates that the cyclical dry-wet process not only reduces the deformation capacity of sandstone but also accelerates energy dissipation. Further support for this conclusion is provided by the strain-dissipated energy curves in Fig. 21c. They show that the relaxation capability of rock samples under dynamic loads will decrease with the increase of dry-wet cycles.



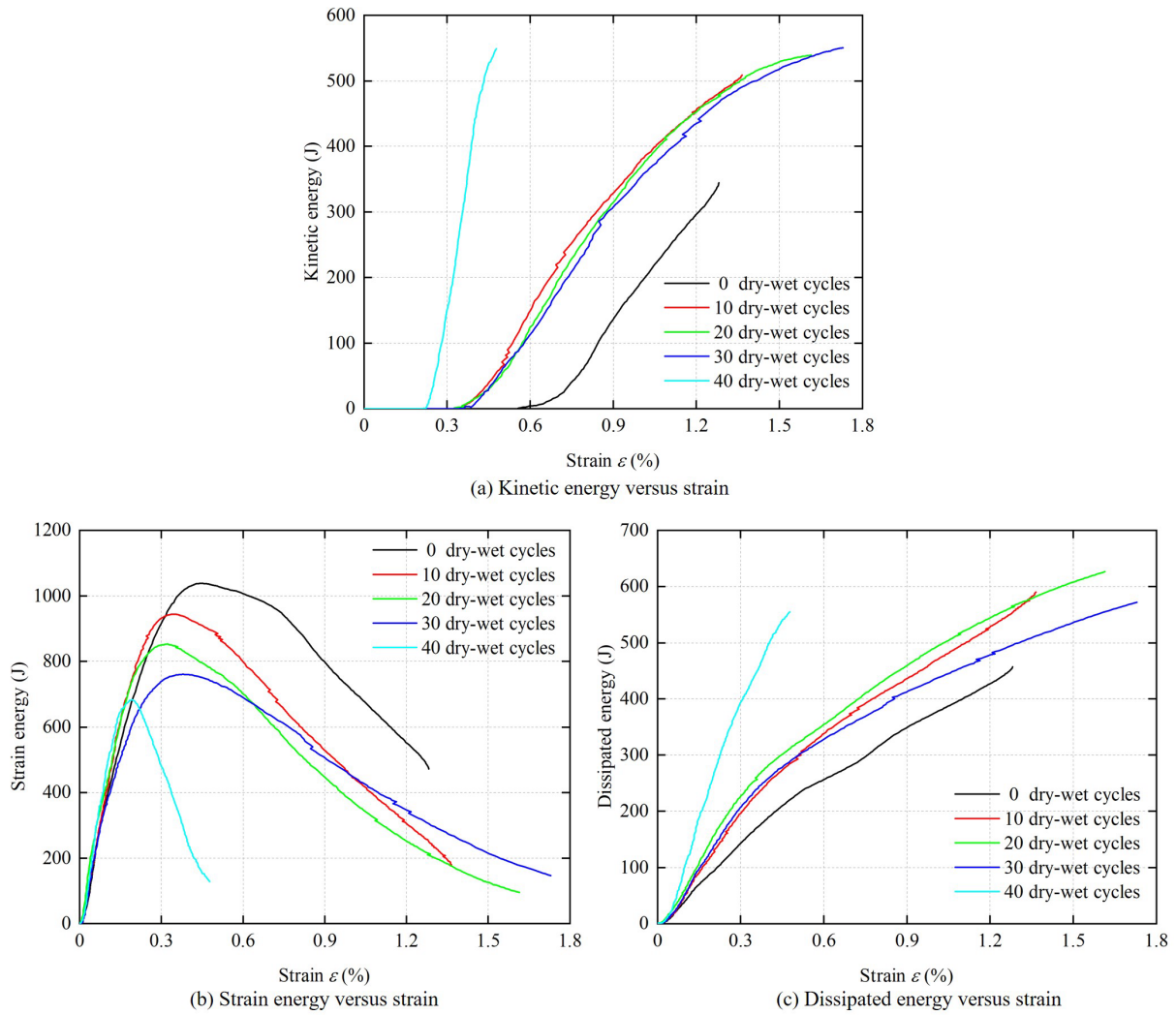


**Fig. 21.** The effect of the dry-wet cycles on the strain-energy curve.

Finally, Fig. 22a–c shows the effect of dry-wet cycles on the three energies as functions of the applied stress. Fig. 22a shows that the stress level at which kinetic energy is first recorded decreases between 0 and 30 dry-wet cycles, and increases slightly between 30 and 40 dry-wet cycles. This confirms that the skeleton structure of rock continuously deteriorates during the 0 to 30 dry-wet cycles, and is slightly enhanced in the next cycles up to 40, due to the high content of quartz minerals. Fig. 22b shows that the peak of strain energy decreases with the dry-wet cycles, and the corresponding stress values follow the same trend. Note, that the rising and falling segments of the stress-energy curves represent the accumulation and release of rock stress, respectively. Therefore, comparing the gyration curvature at the peak point, it can be found that the strain energy consumed per unit of stress gradually decreases with the increase of dry-wet cycles. Fig. 22c shows that the dissipated energy has a higher growth rate in the stress release segment than in the stress accumulation segment. The rate of dissipated energy increases with the dry-wet cycles, indicating that the cyclical dry-wet process disrupts the stress transmission process of rocks, leading to a significant increase in energy consumption due to particle friction and slippage.

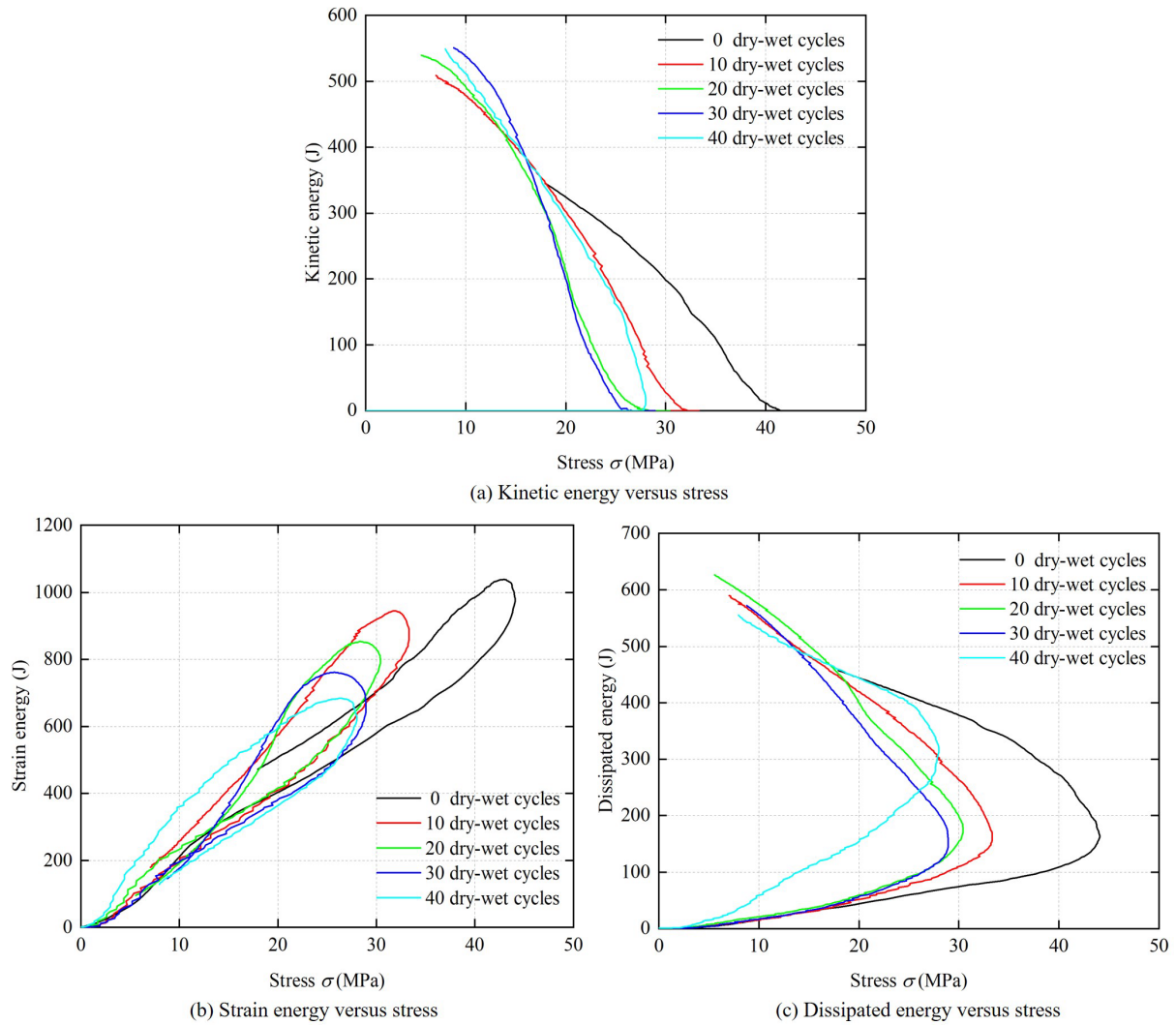
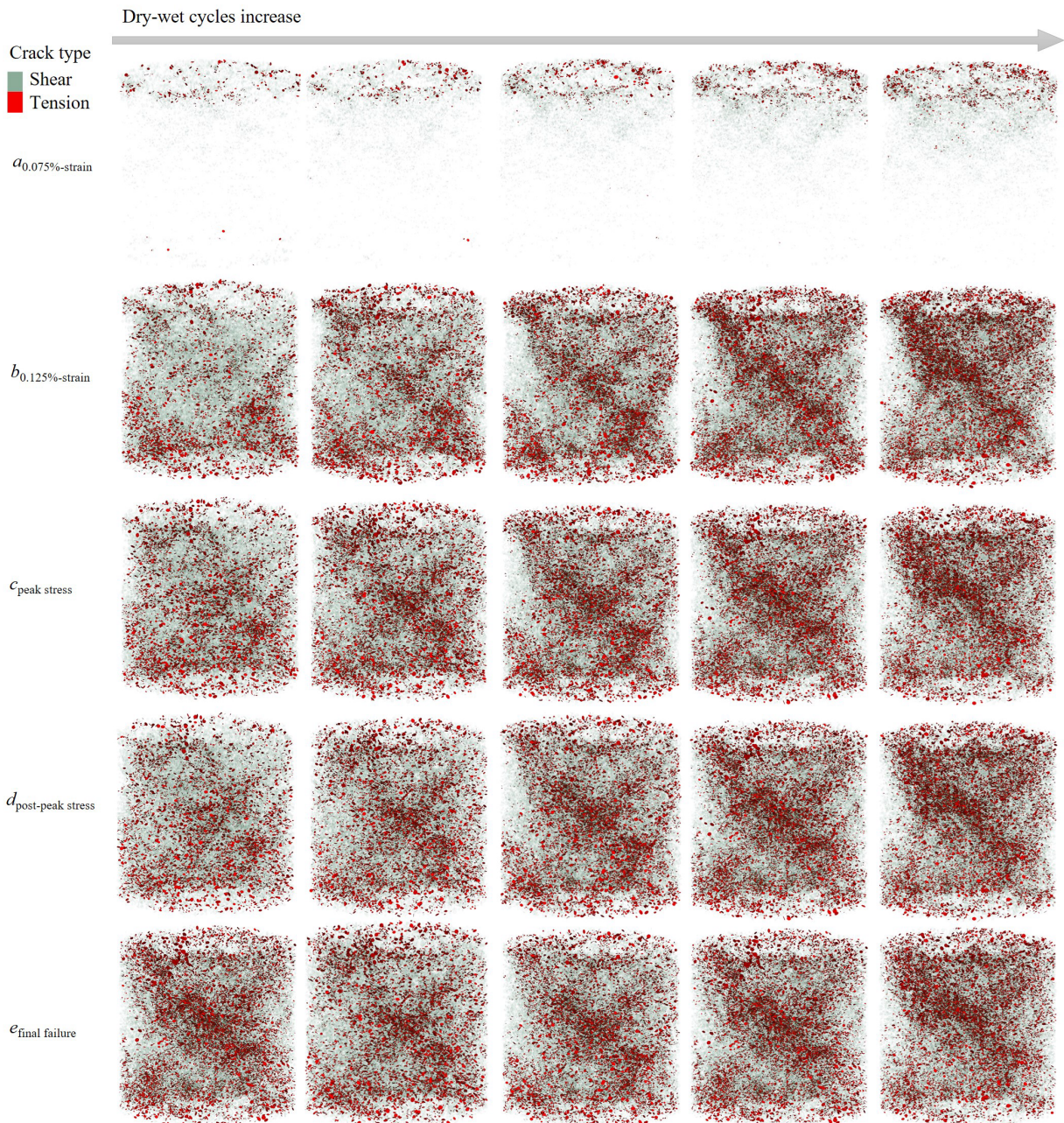


**Fig. 22.** The effect of the dry-wet cycles on the stress-energy curves.

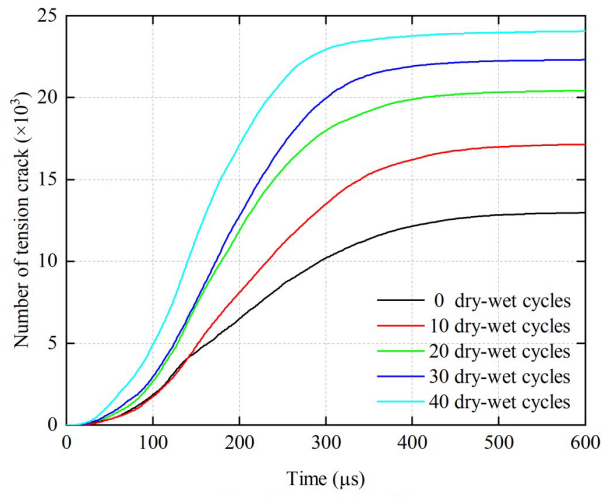
### 5.3. Crack and force chain field

Fig. 23 illustrates the effect of dry-wet cycles on the evolution and distribution of cracks. The cracks initiate at the impact loading surface, primarily in the form of shear cracks. The dry-wet cycles accelerate the rate of crack generation under the same strain conditions but have little effect on the crack field in the post-peak stress segment. The effect of dry-wet cycles on the number of different crack types is given in Fig. 24. The final number of cracks increases with the dry-wet cycles, and the number of shear cracks is always about ten times the number of tensile cracks. The number of shear cracks has similar initial growth rates between 0 and 10 dry-wet cycles, and between 20 and 30 dry-wet cycles, indicating that the degradation process of the rock under dynamic loading conditions exhibits apparent segmented characteristics.

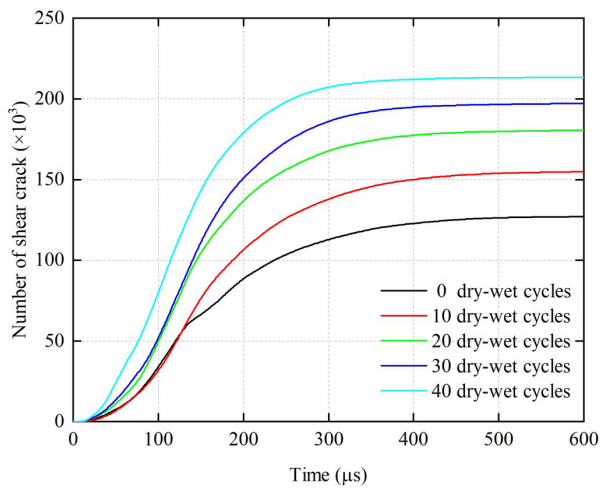
Fig. 25 illustrates the effect of dry-wet cycles on the evolution and distribution of force chains. Considering that the force chain field is three-dimensional, the colour, thickness, and direction, are used to represent the size, density, and direction of the force field respectively. It can be seen in Fig. 25 that with the increase of dry-wet cycles, the force chain field corresponding to points A and B in the pre-peak stress section becomes darker in colour, lower in density, and with an increased mix of directionalities, indicating deterioration of the rock skeleton structure. At the peak stress, the density distribution of the force chain exhibits an abnormal trend with the increase of dry-wet cycles. The rock after 40 dry-wet cycles has the largest fragmentation, hence more contact between fragments, leading to a significant rise in force field density. This persists until the final failure point D, where the force chain density continues to increase with the dry-wet cycles. However, combined with the distribution of the main force chain in Fig. 25, it is evident that the overall directionality and force uniformity deteriorate with increasing dry-wet cycles. Consequently, the main force chain distribution becomes discrete under the action of dry-wet cycles, ultimately resulting in poorer dynamic properties of rock samples.



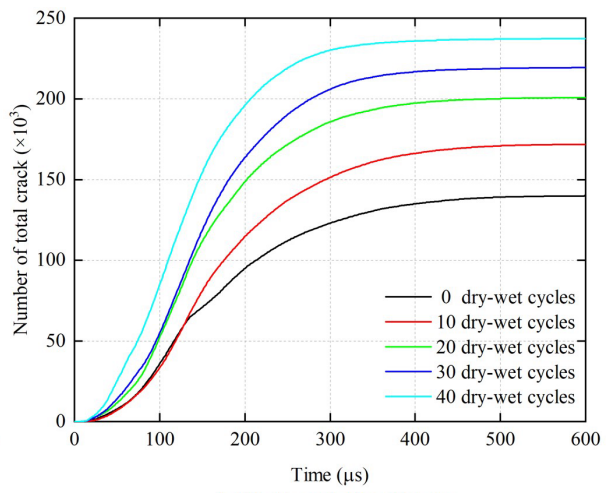
**Fig. 23.** The effect of the dry-wet cycles on the evolution and distribution of crack field.



(a) Tension crack time history



(b) Shear crack time history



(c) Total crack time history

**Fig. 24.** The effect of the dry-wet cycles on the loading time-number curves of cracks.

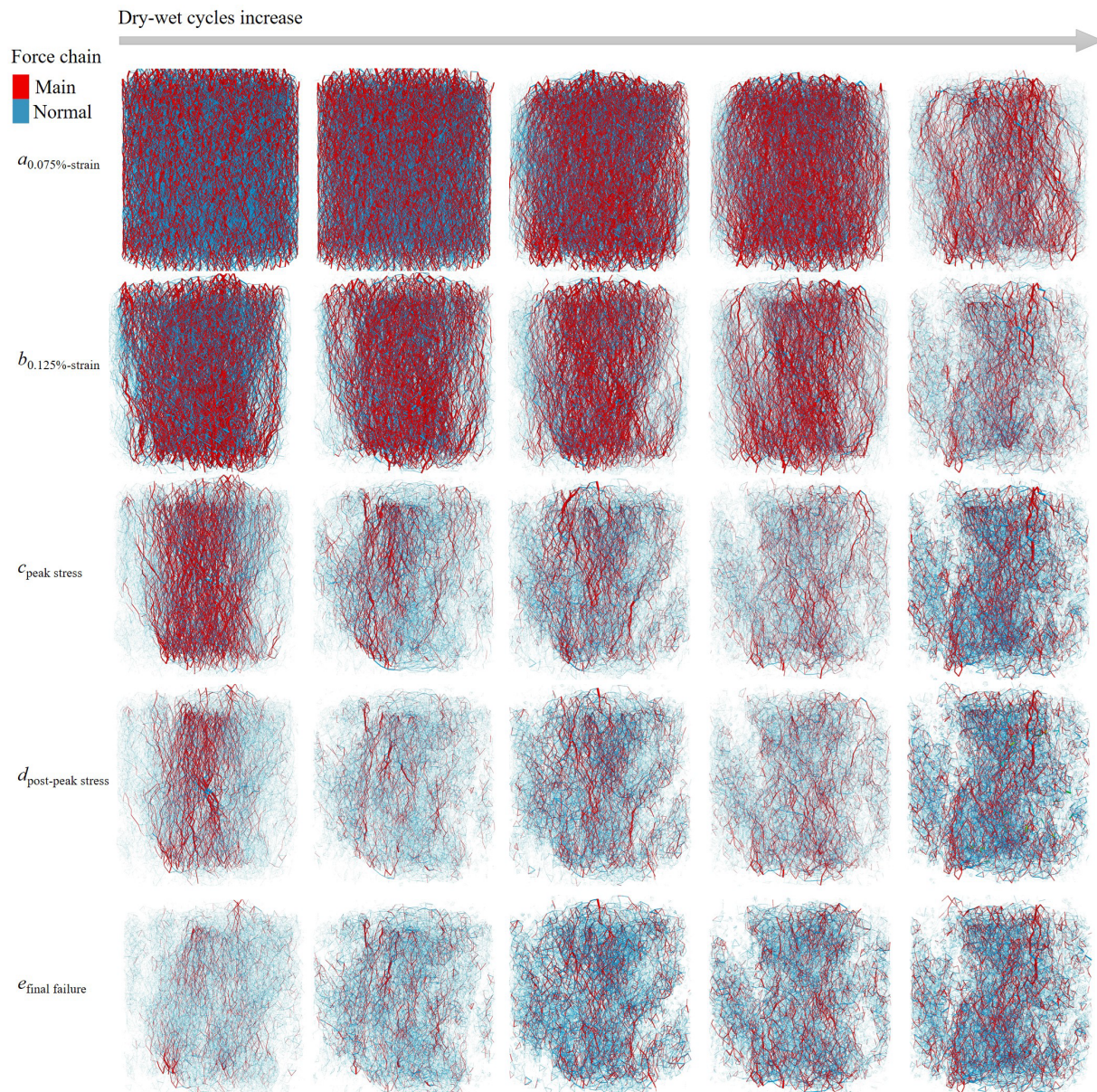


**Fig. 25.** The effect of the dry-wet cycles on the force chain field.

## 6. Conclusions

Experimental and numerical investigation of the effect of dry-wet cycles on the dynamic behaviour of sandstone was performed. SHPB impact tests on sandstone samples subjected to a range of dry-wet cycles were performed to obtain their strain-stress behaviours and fragmental characteristics. These were complemented by MIP and BSE imaging required to understand better the micro-mechanisms of cyclic dry-wet damage and to provide support for the numerical modelling of sandstone samples. Coupled FEM-DEM models of the experimental setups were developed and used to further clarify the effect of dry-wet cycles on the failure features and energy partitions. The main conclusions of the work are:

- (1) The DCS of sandstone samples continuously decreases with the increase of dry-wet cycles; the reduction from 0 to 40 dry-wet cycles is found to be 39.40%. The dependence of DCS on the cycles is fitted with a modified exponential function, which is validated by ultrasonic detection technology. The dry-wet cycles mainly affect the DCS by weakening the elastic limit stress of sandstone, which decreases from 41.75 MPa in 0 dry-wet cycles to 25.62 MPa in 40 dry-wet cycles. The reduction of plastic deformation capacity is small.
- (2) The degree of sandstone fragmentation increases with the dry-wet cycles, and the fragment fractal dimension increases from 2.036 at 0 dry-wet cycle to 2.247 after 40 dry-wet cycles. Within the limitations of the experiments, the largest fragmentation growth occurs after the 23rd dry-wet cycle and the mean life of rock is 25 cycles, predicted by the Logistic model, normal model, and Weibull model.

- (3) The dry-wet cycles increase the porosity by disrupting the original pore structure and distribution. The cyclic dry-wet process affects very differently the macropores and the micro-mesopores. The size uniformity of the macropores increases during the first 20 cycles and then fluctuates, while the size uniformity of the micro- and meso-pores is nearly constant during the first 20 cycles and then increases. This is quantitatively characterized by the Neimark fractal analysis.
- (4) The dry-wet cycles can induce grain boundary failure, edge pores expansion, transgranular cracks, and mineral dissolution, leading to continuous deterioration and final collapse of mineral grains. As the dry-wet cycles progress, the distribution of sandstone particles becomes clear and homogeneous, which is quantitatively described with the statistical parameters of PCAS.
- (5) The numerical simulations provide stress-strain behaviour in agreement with experimental observations and are suitable for investigating additional characteristics of the sandstone behaviour that cannot be measured experimentally. It is found that the dry-wet cycles mainly affect the rate at which strain energy is converted into kinetic energy and dissipated energy, leading to accelerated energy consumption, lower deformation relaxation capability, and disruption of stress transfer.
- (6) The number of generated cracks increases with the dry-wet cycles; shear cracks dominate over tensile cracks. The force chain field and main force chain field become discrete with dry-wet cycles, and the overall directionality and force uniformity deteriorate, representing the progressive failure process of rock materials under the action of dry-wet cycles.

## Acknowledgements

This work was supported by the National Natural Science Foundation of China (Nos. 52374147, 42372328, and U23B2091), National Key Research and Development Program of China (No. 2023YFC3804200) and Xinjiang Uygur Autonomous Region Science and Technology Major Program (No. 2023A01002).

## References

- [1] Amirthan T, Perera MSA. Underground hydrogen storage in Australia: A review on the feasibility of geological sites. *Int J Hydrog Energy* 2023;48(11):4300–28.
- [2] Xie YC, Wu XN, Hou ZM, Li ZY, Luo JS, Lüddeke CT, Huang LC, Wu L, Liao JX. Gleaning insights from German energy transition and large-scale underground energy storage for China's carbon neutrality. *Int J Min Sci Tech* 2023;33(5):529–53.
- [3] Yang K, Fu Q, Yuan L, Liu QJ, He X, Liu FY. Research on development demand and potential of pumped storage power plants combined with abandoned mines in China. *J Energy Storage* 2023;63:106977.
- [4] Colas E, Klopries EM, Tian DY, Kroll M, Selzner M, Bruecker C, Khaledi K, Kukla P, Preuße A, Sabarny C, Schüttrumpf H, Amann F. Overview of converting abandoned coal mines to underground pumped storage systems: Focus on the underground reservoir. *J Energy Storage* 2023;73:109153.
- [5] Bhimaraju A, Mahesh A, Nirbheram JS. Feasibility study of solar photovoltaic/grid-connected hybrid renewable energy system with pumped storage hydropower system using abandoned open cast coal mine: A case study in India. *J Energy Storage* 2023;72:108206.
- [6] Gischig VS. Rupture propagation behavior and the largest possible earthquake induced by fluid injection into deep reservoirs. *Geophys Res Lett* 2015;42(18):7420–8.
- [7] Brito J, Rosa S, Santos J, Sousa J, Pedro A. Socorridos pumping station and water storage tunnel at Madeira Island. *Rock Mechanics and Geo-engineering in Volcanic Environments*. Boca Raton: CRC Press, 2010:271–8.
- [8] Kramer G, Arts T, Urai J, Vrijling H, Huynen J. Risk mitigation and investability of a U-PHS project in the Netherlands. *Energies* 2020;13(19):5072.
- [9] Montero R, Wortberg T, Binias J, Niemann A. Integrated assessment of underground pumped-storage facilities using existing coal mine infrastructure. *Sustainable Hydraulics in the Era of Global Change*. Boca Raton: CRC Press, 2016:953–60.
- [10] Zhang C, Wang FT, Bai QS. Underground space utilization of coalmines in China: A review of underground water reservoir construction. *Tunn Undergr Space Technol* 2021;107:103657.
- [11] Vasarhelyi B. Some observations regarding the strength and deformability of sandstones in dry and saturated conditions. *Bull Eng Geol Environ* 2003;62(3):245–9.
- [12] Hua W, Dong SM, Li YF, Xu JG, Wang QY. The influence of cyclic wetting and drying on the fracture toughness of sandstone. *Int J Rock Mech Min Sci* 2015;78:331–5.
- [13] Zhao ZH, Yang J, Zhang DF, Peng H. Effects of wetting and cyclic wetting–drying on tensile strength of sandstone with a low clay mineral content. *Rock Mech Rock Eng* 2017;50(2):485–91.
- [14] Erguler ZA, Ulusay R. Water-induced variations in mechanical properties of clay-bearing rocks. *Int J Rock Mech Min Sci* 2009;46(2):355–70.
- [15] Wild KM, Walter P, Amann F. The response of Opalinus Clay when exposed to cyclic relative humidity variations. *Solid Earth* 2017;8(2):351–60.
- [16] Bodeux S, Pujades E, Orban P, Brouyère S, Dassargues A. Interactions between groundwater and the cavity of an old slate mine used as lower reservoir of an UPSH (Underground Pumped Storage Hydroelectricity): a modelling approach. *Eng Geol* 2017;217:71–80.
- [17] Khaledi K, Mahmoudi E, Datcheva M, Schanz T. Stability and serviceability of underground energy storage Caverns in rock salt subjected to mechanical cyclic loading. *Int J Rock Mech Min Sci* 2016;86:115–31.

- [18] Guo YT, Yang CH, Mao HJ. Mechanical properties of Jintan Mine rock salt under complex stress paths. *Int J Rock Mech Min Sci* 2012;56:54–61.
- [19] Brantut N, Heap MJ, Meredith PG, Baud P. Time-dependent cracking and brittle creep in crustal rocks: A review. *J Struct Geol* 2013;52:17–43.
- [20] Menéndez J, Fernández-Oro JM, Galdo M, Loredó J. Pumped-storage hydropower plants with underground reservoir: Influence of air pressure on the efficiency of the Francis turbine and energy production. *Renew Energy* 2019;143:1427–38.
- [21] Zhou YX, Xia K, Li XB, Li HB, Ma GW, Zhao J, Zhou ZL, Dai F. Suggested methods for determining the dynamic strength parameters and mode-I fracture toughness of rock materials. *Int J Rock Mech Min Sci* 2012;49:105–12.
- [22] Khanlari G, Abdilor Y. Influence of wet–dry, freeze–thaw, and heat–cool cycles on the physical and mechanical properties of Upper Red sandstones in central Iran. *Bull Eng Geol Environ* 2015;74(4):1287–300.
- [23] Wang TT, Shang B. Three-wave mutual-checking method for data processing of SHPB experiments of concrete. *J MECH* 2014;30(5):N5–N10.
- [24] Jiang HQ, Yi HS, Yilmaz E, Liu SW, Qiu JP. Ultrasonic evaluation of strength properties of cemented paste backfill: Effects of mineral admixture and curing temperature. *Ultrasonics* 2020;100:105983.
- [25] Wu JY, Jing HW, Yin Q, Yu LY, Meng B, Li SC. Strength prediction model considering material, ultrasonic and stress of cemented waste rock backfill for recycling gangue. *J Clean Prod* 2020;276:123189.
- [26] Jing HW, Wu JY, Yin Q, Wang K. Deformation and failure characteristics of anchorage structure of surrounding rock in deep roadway. *Int J Min Sci Technol* 2020;30(5):593–604.
- [27] Gao H, Zhai Y, Wang TN, Li YB, Meng FD, Zhang HQ, Li Y. Compression failure conditions of concrete-granite combined body with different roughness interface. *Int J Min Sci Technol* 2023;33(3):297–307.
- [28] Huang SB, He YB, Liu XW, Xin ZK. Experimental investigation of the influence of dry-wet, freeze-thaw and water immersion treatments on the mechanical strength of the clay-bearing green sandstone. *Int J Rock Mech Min Sci* 2021;138:104613.
- [29] Cherblanc F, Berthonneau J, Bromblet P, Huon V. Influence of water content on the mechanical behaviour of limestone: Role of the clay minerals content. *Rock Mech Rock Eng* 2016;49(6):2033–42.
- [30] Villarraga CJ, Gasc-Barbier M, Vaunat J, Darrozes J. The effect of thermal cycles on limestone mechanical degradation. *Int J Rock Mech Min Sci* 2018;109:115–23.
- [31] Wu JY, Jing HW, Gao Y, Meng QB, Yin Q, Du Y. Effects of carbon nanotube dosage and aggregate size distribution on mechanical property and microstructure of cemented rockfill. *Cem Concr Compos* 2022;127:104408.
- [32] Wu JY, Wong HS, Zhang H, Yin Q, Jing HW, Ma D. Improvement of cemented rockfill by premixing low-alkalinity activator and fly ash for recycling gangue and partially replacing cement. *Cem Concr Compos* 2024;145:105345.
- [33] Åström JA. Statistical models of brittle fragmentation. *Adv Phys* 2006;55(3–4):247–78.
- [34] Blumberg AA. Logistic growth rate functions. *J Theor Biol* 1968;21(1):42–4.
- [35] Ouellet S, Bussière B, Aubertin M, Benzaazoua M. Microstructural evolution of cemented paste backfill: Mercury intrusion porosimetry test results. *Cem Concr Res* 2007;37(12):1654–65.
- [36] Neimark AV. Calculating surface fractal dimensions of adsorbents. *Adsorpt Sci Technol* 1990;7(4):210–9.
- [37] Washburn EW. Note on a method of determining the distribution of pore sizes in a porous material. *Proc Natl Acad Sci USA* 1921;7(4):115–6.
- [38] Rosenbrand E, Fabricius I, Yuan H. Thermally induced permeability reduction due to particle migration in sandstones: the effect of temperature on kaolinite mobilisation and aggregation. In: *Thirty-Seventh Workshop on Geothermal Reservoir Engineering*. Stanford: Stanford University; 2012.
- [39] Yuan P, Wei NN, Ma QY, Chang JC. Coupled effect of water temperature and cyclic wetting and drying on dynamic mechanical characteristics of sandstone. *Adv Civ Eng* 2019;2019:8167651.
- [40] Wang F, Cao P, Cao RH, Xiong XG, Hao J. The influence of temperature and time on water-rock interactions based on the morphology of rock joint surfaces. *Bull Eng Geol Environ* 2019;78(5):3385–94.
- [41] An R, Kong L, Zhang X, Li C. Effects of dry-wet cycles on three-dimensional pore structure and permeability characteristics of granite residual soil using X-ray micro computed tomography. *Journal of Rock Mechanics and Geotechnical Engineering* 2022;14(3):851–60.
- [42] Fang JC, Deng HF, Li JL, Assefa E. Study on the seepage characteristics and degradation mechanism of a single-jointed sandstone under the cyclic dry–wet process in the Three Gorges Reservoir. *Bull Eng Geol Environ* 2021;80(10):8123–36.
- [43] Huang K, Kang B, Zha FS, Li YF, Zhang Q, Chu CF. Disintegration characteristics and mechanism of red-bed argillaceous siltstone under drying–wetting cycle. *Environ Earth Sci* 2022;81(12):336.
- [44] Liu C, Pollard DD, Deng S, Aydin A. Mechanism of formation of wiggly compaction bands in porous sandstone: 1. Observations and conceptual model. *JGR Solid Earth* 2015;120(12):8138–52.
- [45] Potyondy DO. Simulating stress corrosion with a bonded-particle model for rock. *Int J Rock Mech Min Sci* 2007;44(5):677–91.
- [46] Potyondy DO, Cundall PA. A bonded-particle model for rock. *Int J Rock Mech Min Sci* 2004;41(8):1329–64.
- [47] Li XB, Zou Y, Zhou ZL. Numerical simulation of the rock SHPB test with a special shape striker based on the discrete element method. *Rock Mech Rock Eng* 2014;47(5):1693–709.
- [48] Xu Y, Yao W, Wang S, Xia KW. Investigation of the heat-treatment effect on rock fragmentation characteristics using the dynamic ball compression test. *Rock Mech Rock Eng* 2020;53(5):2095–108.
- [49] Hu WR, Liu K, Potyondy DO, Zhang QB. 3D continuum-discrete coupled modelling of triaxial Hopkinson bar tests on rock under multiaxial static-dynamic loads. *Int J Rock Mech Min Sci* 2020;134:104448.